

## Satellite Observations of Mesoscale Eddy-Induced Ekman Pumping

PETER GAUBE,\* DUDLEY B. CHELTON, ROGER M. SAMELSON, MICHAEL G. SCHLAX, AND  
LARRY W. O'NEILL

*College of Earth, Ocean, and Atmospheric Sciences, Oregon State University, Corvallis, Oregon*

(Manuscript received 25 February 2014, in final form 24 September 2014)

### ABSTRACT

Three mechanisms for self-induced Ekman pumping in the interiors of mesoscale ocean eddies are investigated. The first arises from the surface stress that occurs because of differences between surface wind and ocean velocities, resulting in Ekman upwelling and downwelling in the cores of anticyclones and cyclones, respectively. The second mechanism arises from the interaction of the surface stress with the surface current vorticity gradient, resulting in dipoles of Ekman upwelling and downwelling. The third mechanism arises from eddy-induced spatial variability of sea surface temperature (SST), which generates a curl of the stress and therefore Ekman pumping in regions of crosswind SST gradients. The spatial structures and relative magnitudes of the three contributions to eddy-induced Ekman pumping are investigated by collocating satellite-based measurements of SST, geostrophic velocity, and surface winds to the interiors of eddies identified from their sea surface height signatures. On average, eddy-induced Ekman pumping velocities approach  $O(10) \text{ cm day}^{-1}$ . SST-induced Ekman pumping is usually secondary to the two current-induced mechanisms for Ekman pumping. Notable exceptions are the midlatitude extensions of western boundary currents and the Antarctic Circumpolar Current, where SST gradients are strong and all three mechanisms for eddy-induced Ekman pumping are comparable in magnitude. Because the polarity of current-induced curl of the surface stress opposes that of the eddy, the associated Ekman pumping attenuates the eddies. The decay time scale of this attenuation is proportional to the vertical scale of the eddy and inversely proportional to the wind speed. For typical values of these parameters, the decay time scale is about 1.3 yr.

### 1. Introduction

Surface currents associated with mesoscale ocean eddies impart a curl to the surface stress from the relative motion between surface air and water. This surface stress curl has a polarity opposite that of the vorticity of eddy surface currents and thus attenuates eddies by generating Ekman upwelling in the cores of anticyclonic eddies and downwelling in the cores of cyclonic eddies (Dewar and Flierl 1987). An influence of eddy surface vorticity on Ekman pumping has also long been recognized theoretically (Stern 1965). However, direct observations of these two effects on surface currents could

not be obtained before the advent of satellite scatterometers. The first observations of the effects of eddy surface currents on the relative wind (and by inference, the surface stress) were reported by Cornillon and Park (2001) from scatterometer measurements over Gulf Stream rings (see also Park et al. 2006). More recently, McGillicuddy et al. (2007) and Ledwell et al. (2008) showed from scatterometer winds and a tracer released at the depth of the seasonal thermocline that the eddy-induced Ekman upwelling velocity was  $\sim 40 \text{ cm day}^{-1}$  in an anticyclone that they surveyed from ship-based measurements in the subtropical North Atlantic Ocean.

In addition to surface current-induced Ekman pumping, air-sea interaction associated with eddy-induced spatial variations of sea surface temperature (SST) generates a surface stress curl and therefore Ekman pumping that is related primarily to the crosswind SST gradient (Chelton et al. 2004; O'Neill et al. 2010). This air-sea interaction phenomenon is well described in the literature [see, e.g., the reviews by Small et al. (2008), Chelton and Xie (2010), and recent work by O'Neill et al. (2012)]. Briefly, SST modifies the turbulent mixing, drag, and

---

\* Current affiliation: Department of Applied Ocean Physics and Engineering, Woods Hole Oceanographic Institution, Woods Hole, Massachusetts.

---

Corresponding author address: Peter Gaube, Department of Applied Ocean Physics and Engineering, Woods Hole Oceanographic Institution, Mail Stop 9, Woods Hole, MA 02543.  
E-mail: pgaube@whoi.edu

pressure gradients within the marine atmospheric boundary layer. Local changes in surface winds arise from imbalances between the pressure gradient and turbulent stress divergence forces, which generate advective accelerations of near-surface flow from cool to warm SST and decelerations from warm to cool SST. After spatially high-pass filtering to remove large-scale variability, the relationship between SST and wind speed on scales of 100–1000 km (referred to here as the oceanic mesoscale) is approximately linear (O'Neill et al. 2012) and can be quantified by a coupling coefficient that relates the wind speed perturbations to the SST anomalies. This coupling coefficient has been shown to vary somewhat geographically and seasonally with a range of about  $0.2\text{--}0.6\text{ m s}^{-1}\text{ }^{\circ}\text{C}^{-1}$  (O'Neill et al. 2010; O'Neill 2012; O'Neill et al. 2012).

In regions where large-amplitude eddies dominate the mesoscale sea surface height (SSH) variability, eddies have been observed to have SST signatures that closely resemble their SSH structures (e.g., the warm and cold cores in anticyclonic and cyclonic eddies, respectively, in the Gulf Stream region; see Park and Cornillon 2002; Park et al. 2006; Hausmann and Czaja 2012). In regions of less energetic mesoscale eddies, the SST signature associated with westward-propagating eddies is better represented by an asymmetric dipole, with the sign and orientation of the leading (westward) pole being a function of eddy polarity and the background SST gradient (Hausmann and Czaja 2012; see also Fig. 2 below). This is analogous to the dipole structure of near-surface chlorophyll estimated from satellite measurements of ocean color in mesoscale eddies that arises from horizontal advection of the ambient chlorophyll field by the rotational velocity field within the eddy interior (Chelton et al. 2011a). The structures of eddy-induced SST perturbations are quantified globally and for selected regions in this study.

An influence of eddy-induced SST perturbations on the surface wind field was first documented over Gulf Stream rings by Park and Cornillon (2002) from National Aeronautics and Space Administration (NASA) Scatterometer (NSCAT) data and then later from QuikSCAT scatterometer winds by Park et al. (2006). They showed that the eddy-induced SST anomalies associated with Gulf Stream rings generate perturbations in both wind speed and direction. Coupling between SST and wind speed anomalies has been observed over westward-propagating mesoscale features between  $40^{\circ}\text{N}$  and  $40^{\circ}\text{S}$  (Small et al. 2005) and mesoscale eddies of both the South China Sea (Chow and Liu 2012) and Southern Ocean (Frenger et al. 2013). An objective of this study is to show that the well-documented linear relationship between SST and wind speed perturbations in SST frontal regions also occurs over the interiors of midlatitude mesoscale eddies.

Numerous modeling studies have shown that there is a significant reduction of the amplitude and kinetic energy of eddies when the effects of surface currents on the surface stress are accounted for in the surface stress forcing. Eden and Dietze (2009) reported a 50% reduction in eddy kinetic energy (EKE) in their model of the North Atlantic. Hutchinson et al. (2010) and Anderson et al. (2011) reported similar reductions when surface current effects were included. McClean et al. (2011) found that accounting for surface current effects in a fully coupled ocean–atmosphere model resulted in pathways, amplitudes, and lifetimes of large anticyclonic eddies spawned by the Agulhas retroflexion that were more similar to those observed by altimetry when compared to the uncoupled model run.

Ekman pumping associated with the eddy-induced SST influence on surface winds has thus far received much less attention from the modeling community. Jin et al. (2009) found that inclusion of this air–sea interaction reduced the EKE by 25% in a numerical simulation of an idealized eastern boundary current regime. The geographical displacement of the surface stress curl anomalies from the cores of the mesoscale eddies disrupted the approximately axisymmetric structure of the eddies, thus attenuating the mesoscale eddy field. Because the SST signatures of cyclones were stronger than those of anticyclones owing to ageostrophic effects (Jin et al. 2009), cyclones were attenuated more than anticyclones.

While the above three mechanisms for eddy influence on Ekman pumping have been previously identified independently in various studies, their relative importance has not been investigated. An objective of this study is to quantify the magnitudes of the contributions of surface current effects and air–sea interaction to the total eddy-induced Ekman pumping field and to investigate how they vary geographically over the World Ocean.

The relative contributions of SST and the two effects of surface currents to the observed eddy-induced Ekman pumping is investigated by collocating satellite observations of SSH, SST, wind speed, and Ekman pumping to the interiors of mesoscale eddies as identified and tracked from their SSH signatures. The data analyzed in this study are summarized in section 2, along with details of the filtering applied to each variable in order to isolate the eddy signals and the method for collocating them to the eddy interiors. The influence of midlatitude mesoscale eddies on SST and wind speed perturbations is described in section 3. The relative magnitudes of SST and the two contributions to surface current-induced Ekman pumping are explored for an idealized Gaussian eddy in section 4 and compared to observed, eddy-induced Ekman pumping for midlatitude eddies in section 5. Global maps of the magnitudes of SST

and current-induced Ekman pumping are also presented in [section 5](#). Regional variability of the relative importance of SST and current-induced Ekman pumping is presented in [section 6](#). Attenuation of eddies by Ekman pumping, including an estimate of the eddy decay time scale for idealized Gaussian eddies, is discussed in [section 7](#). The results and conclusions are presented in [section 8](#).

## 2. Methods

### a. Eddy-induced Ekman pumping

Wind stress influences the ocean's interior through Ekman pumping. With the Ekman transport modified by the surface geostrophic vorticity  $\zeta$  following [Stern \(1965\)](#), the total Ekman pumping is

$$W_{\text{tot}} = \frac{1}{\rho_o} \nabla \times \left[ \frac{\boldsymbol{\tau}}{(f + \zeta)} \right] \approx \frac{\nabla \times \boldsymbol{\tau}}{\rho_o(f + \zeta)} + \frac{1}{\rho_o(f + \zeta)^2} \left( \tau^x \frac{\partial \zeta}{\partial y} - \tau^y \frac{\partial \zeta}{\partial x} \right), \quad (1)$$

where  $\rho_o = 1020 \text{ kg m}^{-3}$  is the (assumed constant) surface density of seawater,  $f = 2\Omega \cos\theta$  is the Coriolis parameter for latitude  $\theta$  and Earth rotation rate  $\Omega$ , and the surface stress  $\boldsymbol{\tau}$  has zonal and meridional components  $\tau^x$  and  $\tau^y$ , respectively. In addition to the effect on Ekman pumping from the vorticity  $\zeta$ , eddies may induce Ekman pumping through their effect on local surface stress, either through the influence of eddy surface currents on the local relative wind (see below) or through air–sea coupling arising from eddy-induced modifications of local SST. The contribution to the total Ekman pumping that arises from the meridional derivative of the Coriolis parameter ( $\beta$ ), and is proportional to the zonal stress  $\tau^x$ , has been neglected in (1). An eddy-induced component of this term arises from the eddy influence on surface stress. However, for a large-scale background zonal wind with a representative speed of  $7 \text{ m s}^{-1}$ , this eddy-induced component is only of order 2% of the nominal  $2 \text{ cm day}^{-1}$  magnitude of the mean term and is therefore negligible.

In the bulk aerodynamic approximation, the surface stress  $\boldsymbol{\tau}$  is related to the relative wind  $\mathbf{u}_{\text{rel}}$  through an equation of the form

$$\boldsymbol{\tau} = \rho_a C_D \mathbf{u}_{\text{rel}} |\mathbf{u}_{\text{rel}}|, \quad (2)$$

where  $\rho_a$  is the air density (considered here to be constant and equal to  $1.2 \text{ kg m}^{-3}$ ), and  $C_D$  is a drag coefficient. Here, the relative wind  $\mathbf{u}_{\text{rel}}$  is expressed as

$$\mathbf{u}_{\text{rel}} = \mathbf{u}_a - \mathbf{u}_o, \quad (3)$$

where  $\mathbf{u}_a$  is the absolute vector wind, and  $\mathbf{u}_o$  is the vector surface ocean current. Coherent eddy structures have

associated surface velocities  $\mathbf{u}_o$  that systematically modify the relative wind  $\mathbf{u}_{\text{rel}}$  and therefore also the surface stress  $\boldsymbol{\tau}$ .

Persistent mesoscale SST variations have been shown to have systematic effects on the local surface stress, with increased stress found over relatively warm water and decreased stress over cool water [see the reviews by [Small et al. \(2008\)](#) and [Chelton and Xie \(2010\)](#)]. Consequently, an SST-induced surface stress curl has been shown to exist that is linearly related to the local crosswind SST gradient in SST frontal regions ([Chelton et al. 2004](#); [O'Neill et al. 2012](#); and references therein). To estimate the eddy SST-induced Ekman pumping, we utilized the empirical linear relationship between the perturbation surface stress curl  $\nabla \times \boldsymbol{\tau}'$  and the crosswind components of the SST gradient:

$$\nabla \times \boldsymbol{\tau}'_{\text{SST}} = -\alpha_c^{\text{strcurl}} \left( \frac{\partial T}{\partial n} \right)', \quad (4)$$

where  $\alpha_c^{\text{strcurl}}$  is a coupling coefficient,  $\partial T / \partial n$  is the crosswind SST gradient (see [section 2e](#)), and the primes denote a spatial high-pass filtering with  $6^\circ \times 6^\circ$  half-power filter cutoffs to isolate the mesoscale air–sea interaction.

We decompose the total Ekman pumping [(1)] by separating the stress curl term into components deriving from the eddy SST and the eddy surface current effects to obtain an approximation  $\tilde{W}_{\text{tot}}$  to  $W_{\text{tot}}$ :

$$\tilde{W}_{\text{tot}} = W_c + W_\zeta + W_{\text{SST}}, \quad (5)$$

$$W_c = \frac{\nabla \times \tilde{\boldsymbol{\tau}}}{\rho_o(f + \zeta)}, \quad (6)$$

$$W_\zeta = \frac{1}{\rho_o(f + \zeta)^2} \left( \tilde{\tau}^x \frac{\partial \zeta}{\partial y} - \tilde{\tau}^y \frac{\partial \zeta}{\partial x} \right), \quad \text{and} \quad (7)$$

$$W_{\text{SST}} = \frac{\nabla \times \boldsymbol{\tau}'_{\text{SST}}}{\rho_o(f + \zeta)}. \quad (8)$$

Here,  $W_c$  is the Ekman pumping induced by the local surface current effect on the relative wind ([Dewar and Flierl 1987](#)). The latter may be conceived of as the difference between a smooth, large-scale, “background” wind field  $\mathbf{u}_{\text{bg}}$  and the eddy surface current  $\mathbf{u}_o$ , so that the stress on which  $W_c$  depends may be written as

$$\tilde{\boldsymbol{\tau}} = \rho_a C_D (\mathbf{u}_{\text{bg}} - \mathbf{u}_o) |\mathbf{u}_{\text{bg}} - \mathbf{u}_o|, \quad (9)$$

where the tilde indicates the surface stress resulting only from eddy surface currents  $\mathbf{u}_o$  and the large-scale, background wind  $\mathbf{u}_{\text{bg}}$ . The quantity  $W_\zeta$  is the Ekman pumping induced by the dependence of Ekman transport on the local vorticity  $f + \zeta$  ([Stern 1965](#)).

The derivation of  $\tilde{W}_{\text{tot}}$  from  $W_{\text{tot}}$  contains several approximations. The nonlinear dependence of the stress on relative wind is effectively neglected in the separation of stress into SST-induced and surface current-induced components and in the specification of the surface current-induced Ekman component in terms of a smooth—and therefore, implicitly, spatially filtered—background wind field. In addition, the specification of  $W_{\text{SST}}$  is itself empirical based on the coupling coefficient  $\alpha_c^{\text{strcl}}$  in (4).

A total current-induced contribution  $W_{\text{cur}}$  to the eddy-induced Ekman pumping may be defined as

$$W_{\text{cur}} = W_c + W_\zeta. \quad (10)$$

The first contribution to total current-induced Ekman pumping,  $W_c$  from (6), resulting from the curl of the surface stress (with the Coriolis parameter modified by the local surface vorticity) is sometimes referred to as “linear Ekman pumping” (e.g., McGillicuddy et al. 2008). This portion of the total Ekman pumping, which we will refer to as surface stress curl-induced Ekman pumping, generates upwelling in anticyclonic mesoscale ocean eddies and downwelling in cyclonic mesoscale ocean eddies (see section 4b). The second contribution to total current-induced Ekman pumping,  $W_\zeta$  from (7), which we will refer to as vorticity gradient-induced Ekman pumping, results from the interaction of the surface stress with the surface current vorticity gradient and generates a dipole of Ekman upwelling and downwelling within the interiors of mesoscale eddies. This has been called “nonlinear Ekman pumping” (e.g., McGillicuddy et al. 2008). The relative sizes of these two contributions to the total current-induced Ekman pumping [(10)] are estimated in section 4b where it is determined that  $W_c$  and  $W_\zeta$  are comparable in magnitude, but different in spatial structures.

Our objective is to assess and quantify the different contributions to eddy-induced Ekman pumping that arise from the surface current effect, the surface vorticity effect, and the SST effect. Our approach is to compute the corresponding approximate terms  $W_c$ ,  $W_\zeta$ , and  $W_{\text{SST}}$  from observations of SST, SSH with the geostrophic approximation, and spatially filtered observational estimates of surface winds, all of which are collocated to the interiors of eddies identified and tracked by their SSH signatures. We analyze the resulting estimates and their relative contributions to the sum  $\tilde{W}_{\text{tot}}$ . We then further compute the total eddy-induced Ekman pumping  $W_{\text{tot}}$  directly from (1), using scatterometer estimates of surface winds, supplemented by the same geostrophic SSH estimates of  $\zeta$  used to compute  $W_\zeta$  and compare this direct and essentially

independent estimate  $W_{\text{tot}}$  to the sum  $\tilde{W}_{\text{tot}}$  of the three approximated components. The observational datasets and detailed methodology for these calculations are described below in sections 2b–e. We conduct the analysis both over the global midlatitudes and subsequently for a selected set of subregions representing distinctive oceanographic regimes.

#### b. Sea surface height, geostrophic currents, and eddy tracking

The investigation of eddy-induced Ekman pumping within mesoscale eddies requires the identification and tracking of eddies. As described in detail in appendix B of Chelton et al. (2011b), mesoscale eddies were identified and tracked based on closed contours of SSH. The altimeter-tracked eddy dataset used in this analysis is available online (at <http://cioss.coas.oregonstate.edu/eddies>). The merged SSH fields used here are the reference series dataset obtained from Collecte Localis Satellites [CLS/Archiving, Validation, and Interpretation of Satellite Oceanographic (AVISO)]. This SSH dataset was constructed by smoothing the Ocean Topography Experiment (TOPEX)/Poseidon or *Jason-1* measurements with *ERS-1*, *ERS-2*, or *Envisat* (Ducet et al. 2000) onto a  $1/4^\circ \times 1/4^\circ$  global grid at 7-day intervals. These merged SSH measurements afford spatial resolution that is sufficient to enable the identification and tracking of mesoscale ocean eddies; the wavelength resolution of the merged SSH fields is about  $2^\circ$  in latitude by  $2^\circ$  in longitude, which corresponds to a feature radius resolution of about 40 km for quasi-Gaussian eddies (Chelton et al. 2011b). As discussed below, this analysis also uses wind measurements from the SeaWinds scatterometer onboard the QuikSCAT satellite and SST measurements derived from the Advanced Microwave Scanning Radiometer for Earth Observing System (EOS) (AMSR-E) sensor onboard the EOS *Aqua* satellite and thus is restricted to the 7.5-yr time period from July 2002 to November 2009 for which all three of the SSH, wind, and SST datasets overlap.

Tracked eddies are characterized by several variables. The eddy amplitude at each weekly time step along its trajectory is defined to be the difference between the SSH extremum in the eddy interior and the SSH value along the eddy perimeter, delineated as the outermost closed contour of SSH that defines a compact structure. The eddy interior is defined to be the region inside this SSH contour. The rotational speed  $U$  of an eddy is characterized at each point along its trajectory as the average geostrophic speed along the SSH contour around which the average geostrophic speed is maximum within the eddy interior. The horizontal speed-based radius scale  $L_s$  of the eddy is defined to be the



radius of a circle with area equal to that enclosed by this SSH contour.

For the eddy dataset considered here, the global (midlatitude) mean values of amplitude,  $U$ , and  $L_s$  are 6.7 cm, 16.1 cm s<sup>-1</sup>, and 90 km, respectively. Global distributions of these variables are similar for anticyclones and cyclones (Fig. 1). Regional distributions can depart significantly from the global mean. For example, eddies in the Agulhas Return Current (ARC) are large in amplitude when compared to the global mean (Fig. 1a; Table 1). In the Caribbean Sea (CAR), eddies have comparatively large radius scales (Fig. 1b; Table 1). In the South Pacific (SPO), eddies are small in amplitude and large in radius, resulting in relatively slow rotational speeds compared to the average of midlatitude eddies (Figs. 1a–c; Table 1).

The SST and wind fields described below in sections 2c–e were collocated to the interiors of the eddies identified from their SSH signatures. Composite averages of the relevant fields were constructed for midlatitude (15°–45°) eddies in both hemispheres. In total, 8254 cyclonic and 7668 anticyclonic midlatitude eddies with lifetimes of 12 weeks or longer satisfied this criterion during the 7.5-yr study period. Our consideration only of eddies with lifetimes of 12 weeks and longer is an attempt to focus on isolated coherent vortices and not current meanders, which can resemble eddies in the spatially high-pass filtered SSH fields but usually retain compact structures for time periods shorter than 12 weeks. The compositing was done on a common grid by scaling the distances from the eddy SSH extremum to each 1/4° grid point in the eddy interior by the eddy radius  $L_s$ . Each normalized grid location was then interpolated onto a high-resolution grid for normalized zonal and meridional coordinates ranging from -2 to 2.

For the selected study regions investigated in section 6, composites within eddy interiors include only the times when the eddy SSH extremum is located within the latitude–longitude bounds of each region. Observations associated with a given eddy are excluded from composites prior to or after the eddy propagation within the study region.

### c. Relative winds and surface stress

Vector winds and stress were estimated from rain-free 10-m wind measurements by the SeaWinds scatterometer onboard the QuikSCAT satellite. The QuikSCAT mission began on 19 July 1999 and ended on 23 November 2009. Scatterometers infer surface stress from radar backscatter (e.g., Ross et al. 1985; Chelton and Freilich 2005). These winds are reported as the equivalent neutral vector wind at 10 m relative to the moving sea surface, that is, the relative wind that would be associated with

the observed surface stress if the boundary layer were neutrally stratified (Liu and Tang 1996). The stress and equivalent neutral wind are thus related by a neutral stability drag coefficient. Note that this does not imply that scatterometry assumes neutrally stable conditions.

The rain-free QuikSCAT estimates of equivalent neutral relative wind  $\mathbf{u}_{\text{rel}}$  used here are the Remote Sensing Systems version 4 dataset (Lucrezia and Wentz 2011). The swath data were interpolated onto a 1/4° × 1/4° grid using a spatial smoother with a half-power filter cutoff of 80 km. Observations within ~100 km of the swath edge were excluded to reduce directional ambiguities and avoid problems with spatial derivatives near the swath edges.

The surface stress  $\boldsymbol{\tau}$  was estimated from the QuikSCAT equivalent neutral relative winds using the bulk formulation in (2). The neutral drag coefficient  $C_D$  used here is based on the bulk flux formulation from the Coupled Ocean–Atmosphere Response Experiment, version 3.0 (COARE 3.0; Fairall et al. 2003). Surface stresses computed by the COARE 3.0 algorithm are about 15% larger than those computed by the Large et al. (1994) algorithm (see Fig. B2 of Risien and Chelton 2008), but the conclusions of this study are not significantly dependent on the choice of  $C_D$ .

The surface stress  $\boldsymbol{\tau}$ , stress components  $\tau^x$  and  $\tau^y$ , and vector winds were calculated in swath on a 1/4° by 1/4° grid. The surface stress curl  $\nabla \times \boldsymbol{\tau}$  was computed in swath using centered finite differences of  $\tau^x$  and  $\tau^y$ . Daily averages of the surface stress, stress components, stress curl, wind speed, and vector winds were computed and subsequently smoothed in time as described below. To be commensurate with the ~35-day  $e$ -folding time scale of the covariance function of the objective analysis procedure used by AVISO to process the SSH fields (Ducet et al. 2000; see also appendix A.2 of Chelton et al. 2011b), the various wind fields considered in this study were constructed at the same 7-day intervals as the SSH observations using temporal low-pass filtering with a half-power filter cutoff of 30 days. At the scales of ocean basins, Ekman pumping velocities are  $O(10)$  cm day<sup>-1</sup> (Leetmaa and Bunker 1978; Risien and Chelton 2008). To isolate the influence of mesoscale ocean eddies on Ekman pumping, the direct estimate [(1)] of Ekman pumping was spatially high-pass filtered to remove large-scale features unrelated to the mesoscale variability that is of interest in this study. After some experimentation, half-power filter cutoffs of 6° longitude by 6° latitude were chosen as a compromise between attenuating unwanted large-scale atmospheric variability and retaining variability at the oceanic mesoscales. The perturbation wind speed fields analyzed in

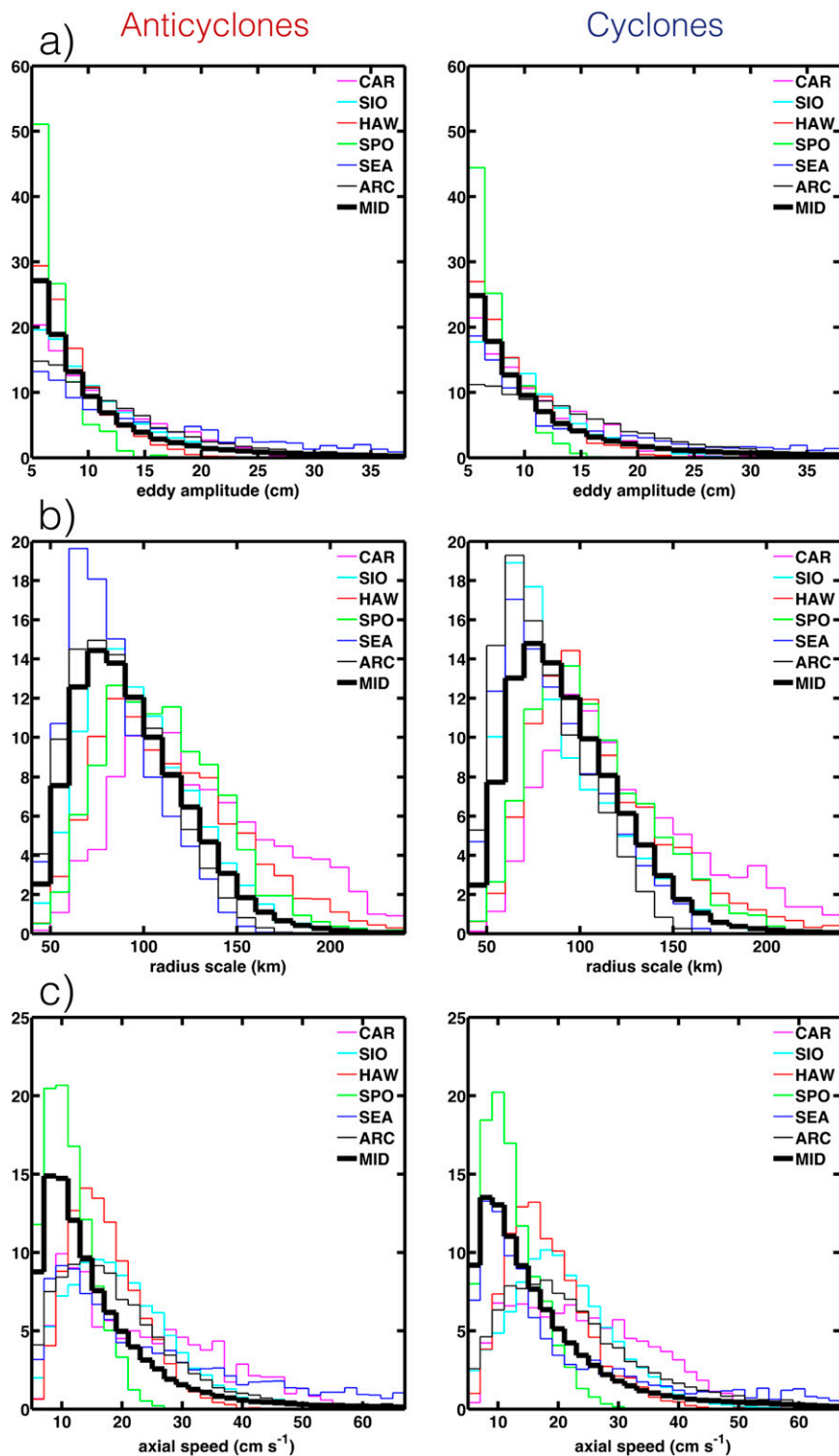


FIG. 1. Histograms of (a) eddy amplitude, (b) speed-based eddy radius scale  $L_s$  and (c) eddy rotational speed  $U$  for (left) anticyclones and (right) cyclones for each of the 6 study regions (CAR: Caribbean Sea; SIO: south Indian Ocean; HAW: Hawaiian Ridge; SPO: South Pacific Ocean; SEA: southeast Atlantic; ARC: Agulhas Return Current) and all midlatitude eddies (MID: thick black line).

TABLE 1. Overview of mesoscale eddy statistics for each of the six study regions. Counts and mean values are reported as cyclones/anticyclones.

	CAR	SIO	HAW	SPO	SEA	ARC	Midlatitude
No. eddies	145/96	402/350	295/255	254/224	167/177	787/748	8204/4614
No. realizations	1693/1230	9615/8710	5121/4516	4452/3463	2386/2962	16 000/15 000	204 000/203 000
$A$ (cm)	8.0/7.8	8.5/8.5	6.9/6.3	4.2/3.7	12.5/15.3	13.6/11.7	8.1/7.3
$L_S$ (km)	125/133	90/97	110/115	106/110	86/83	81/87	93/94
$U$ (cm s <sup>-1</sup> )	24.3/23.6	21/20	18.3/17.3	12.2/11.3	24/28	23.3/20.7	17.8/16.2

section 3 were spatially high-pass filtered in the same manner.

Composites of  $W_{\text{tot}}$  were computed from (1) based on QuikSCAT measurements of surface stress and velocity derived from SSH, estimated here from centered finite differences of the SSH fields on the  $1/4^\circ \times 1/4^\circ$  grid. Computation of the relative vorticity  $\zeta = \partial v/\partial x - \partial u/\partial y$  thus consists of the second derivatives of SSH. Computation of  $\partial\zeta/\partial x$  and  $\partial\zeta/\partial y$  consists of the third derivatives of SSH. Any noise in the SSH is considerably amplified in the derivative operations.

#### d. Estimation of surface current-induced Ekman pumping

The eddy surface current and vorticity in the expressions (9) for  $\tilde{\tau}$  and (6)–(8) for the three components of  $\tilde{W}_{\text{tot}}$  were estimated from the geostrophic surface currents computed from the AVISO SSH fields. The large-scale, absolute background wind field  $\mathbf{u}_{\text{bg}}$  in (9) was estimated by smoothing the QuikSCAT vector winds to remove variability with wavelength scales shorter than  $6^\circ$ .

The curl of the current-induced stress [(9)] was estimated using centered finite differencing. Note that  $W_{\text{cur}}$  does not include any SST effects on the surface stress  $\tau$ . The current-induced Ekman pumping fields estimated from (10) were spatially high-pass filtered to attenuate variability with wavelengths longer than  $6^\circ$ . This spatial high-pass filtering is necessary to isolate eddy-induced Ekman pumping from the basin-scale Ekman pumping generated by the large-scale background wind field. When averaged over the interiors of all midlatitude eddies, the absolute value of the residual large-scale Ekman pumping estimated from the smoothed background wind field  $\mathbf{u}_{\text{bg}}$  alone [i.e., for stress from (9) with  $\mathbf{u}_o = 0$  everywhere] is  $O(1)$  cm day<sup>-1</sup>.

#### e. Estimation of SST-induced Ekman pumping

The SST fields used in this study are the optimally interpolated SST analyses produced by the National Oceanic and Atmospheric Administration (NOAA) National Climatic Data Center. Microwave and infrared satellite observations were combined with in situ measurements of SST to obtain daily, global fields on a  $1/4^\circ \times 1/4^\circ$  grid

(Reynolds et al. 2007). To isolate variability on oceanic mesoscales, the daily fields of SST were temporally and spatially filtered in the same manner described in section 2c for the QuikSCAT wind observations.

For the computation of the SST-induced Ekman pumping, the crosswind SST gradient was calculated from the meridional ( $\partial T/\partial y$ ) and zonal ( $\partial T/\partial x$ ) SST gradient components by

$$\frac{\partial T}{\partial n} = -\sin\psi \frac{\partial T}{\partial x} + \cos\psi \frac{\partial T}{\partial y}, \quad (11)$$

where  $n$  is the local crosswind spatial coordinate, oriented  $90^\circ$  counterclockwise from the wind direction  $\psi$  that is estimated from individual orbital passes of QuikSCAT. Weekly fields of the resultant crosswind SST gradient were constructed at the same 7-day intervals as the SSH observations with temporal low-pass filtering with a half-power filter cutoff of 30 days. These weekly fields were then spatially high-pass filtered with half-power filter cutoffs of  $6^\circ$  longitude by  $6^\circ$  latitude to isolate mesoscale variability to obtain  $(\partial T/\partial n)'$  in (4).

O'Neill et al. (2012) showed that the coupling between the perturbation surface stress and SST is highly variable, both regionally and temporally, depending primarily on the magnitude of the background surface stress field. The temporal variability is not completely understood, and temporally varying, empirically determined, coupling coefficients can result in nonphysical negative relationships between the crosswind SST gradient and perturbations of the surface stress curl. For present purposes of assessing the magnitude of SST-induced surface stress curl, the fields were therefore estimated from temporally constant coupling coefficients  $\alpha_c^{\text{strcl}}$  computed separately for each region considered in sections 5–6, with a global (midlatitude) mean coupling coefficient  $\alpha_c^{\text{strcl}} = 0.013 \text{ N m}^{-2} \text{ }^\circ\text{C}^{-1}$  (Table 2).

For the regional analysis in section 6, the coupling coefficients are defined to be the regression coefficients obtained by regressing  $\nabla \times \tau'$  onto  $-\partial T/\partial n$ . These regression coefficients can be obtained from

$$\alpha_c^{\text{strcl}} = \rho_c \frac{\sigma_{\text{strcl}}}{\sigma_c}, \quad (12)$$

TABLE 2. Coupling coefficients of surface stress curl perturbation to the crosswind SST gradient anomalies  $\alpha_c^{\text{strcurl}}$  ( $\text{N m}^{-2} \text{ } ^\circ\text{C}^{-1}$ ) and wind speed perturbation to SST anomalies  $\alpha_{\text{spd}}^{\text{SST}}$  ( $\text{m s}^{-1} \text{ } ^\circ\text{C}^{-1}$ ).

Region	$\alpha_c^{\text{strcurl}}$	$\alpha_{\text{spd}}^{\text{SST}}$
CAR	0.013	0.35
SIO	0.0088	0.25
HAW	0.0093	0.21
SPO	0.0069	0.15
SEA	0.019	0.41
ARC	0.025	0.44
Midlatitudes	0.013	0.28

where  $\rho_c$  is the cross correlation between  $\nabla \times \tau'$  and  $-\partial T/\partial n$ , and  $\sigma_{\text{strcurl}}$  and  $\sigma_c$  are the standard deviations of  $\nabla \times \tau'$  and  $\partial T/\partial n$ , respectively.

### 3. Eddy-induced perturbations of SST and relative wind speed

Eddy surface currents influence SST predominantly by horizontal advection of the background SST field (Fig. 2) resulting in dipolar SST anomalies, whose sign and orientation depend on both the direction of the background SST gradient and the rotational sense of the eddy. In this section, composite averages of mesoscale SST anomalies are examined in a rotated frame of reference determined by the orientation of the large-scale SST gradient. A large-scale SST gradient field was defined as the gradient of the  $6^\circ \times 6^\circ$  smoothed SST fields. The SST gradient direction for each eddy realization was defined as the average direction of this large-scale SST gradient over a  $4^\circ \times 4^\circ$  box centered on the eddy SSH extremum. When this large-scale SST gradient vector had a nonzero northward (southward) component, the SST anomalies were rotated to orient the large-scale SST gradient vector at a polar angle of  $90^\circ$  ( $-90^\circ$ ) prior to composite averaging.

The importance of composite averaging the SST anomalies in a rotated coordinate system defined by the gradient of the large-scale (spatially smoothed) SST field is clear from the schematic diagrams in Figs. 2a and 2b. Composites calculated from nonrotated coordinates would blur the horizontal dipole structure of the eddy-induced SST perturbations because of temporal and geographical variability in the direction of the SST gradient vector and hence the orientation of the anomaly SST dipole.

The dipole structure shown schematically in Fig. 2 is readily apparent in the eddy composites of the SST anomalies in rotated coordinates shown in Figs. 3a and 3b. The two poles are strongly asymmetric along axes that are rotated relative to the isotherms of the large-scale SST field. For the case of a clockwise-rotating eddy propagating westward in a region of southward SST gradient,

the northward velocity on the western side of the eddy advects warmer water from the southwestern quadrant to the northwestern quadrant, resulting in a positive SST anomaly in the northwestern quadrant<sup>1</sup> (Fig. 3a, left panel). The clockwise-rotating surface currents on the trailing side of the eddy advect relatively cool water from the northeastern quadrant to the southeastern quadrant, resulting in a negative SST anomaly in the southeastern quadrant. The opposite is true for clockwise-rotating eddies propagating in regions with a background SST gradient that has a nonzero northward component (Fig. 3b, left panel). For counterclockwise rotation (Figs. 3a,b, right panels), the responses are very similar, but reflected meridionally and reversed with respect to the direction of the SST gradient.

The dipole patterns of anomalous SST within the interiors of midlatitude eddies, which have been observed previously in the North Atlantic and Southern Ocean by Hausmann and Czaja (2012), result from a combination of the rotational sense of the eddies, the direction of the background SST gradient, and the eddy propagation direction. The latter accounts for the asymmetry between the magnitudes of the poles in the leading (western) and trailing (eastern) sides of the eddies. The anomalies in the trailing side are generally weaker and noisier, likely as a result of the trailing half of the eddy encountering a field that has been disturbed by the leading half (Chelton et al. 2011a).

The composites of SST within midlatitude eddies (Figs. 3a,b) thus show cold and warm interiors in cyclones and anticyclones, respectively. However, the common notion of “cold-core cyclones” and “warm-core anticyclones” is not as simple as is often presumed. In particular, the centers of the cold and warm SST anomalies of the primary poles of the composites are displaced westward and either northward or southward relative to the eddy composite SSH extremum. Moreover, they are paired with an SST anomaly of opposite sign and much smaller magnitude on the opposite side of the eddy extremum.

It is noteworthy that the large-scale SST gradients are predominantly southward in the Northern Hemisphere and northward in the Southern Hemisphere. This hemispheric bias in the direction of the background SST gradient is reflected in the fact that approximately 99% of the midlatitude eddies in a southward SST gradient in Fig. 3a are in the Northern Hemisphere. Likewise, 98% of

<sup>1</sup> Note that the quadrants referred to here are relative to the rotated coordinate system in which the large-scale background SST gradient is oriented at polar angles of  $90^\circ$  and  $-90^\circ$  for SST fields with, respectively, a northward and southward component of the gradient vector.

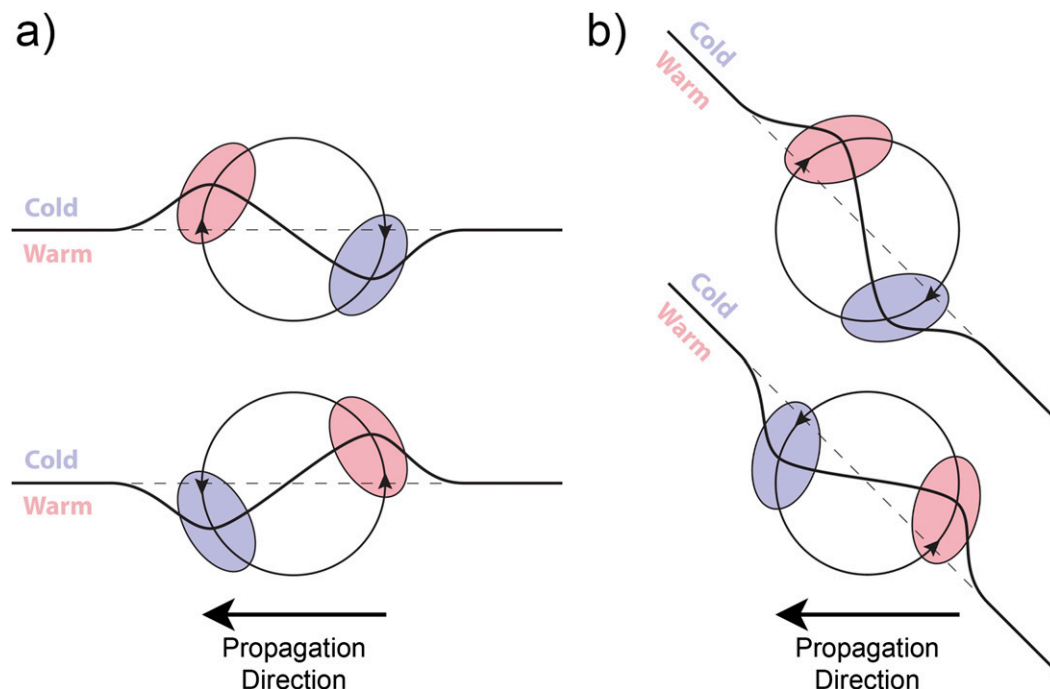


FIG. 2. Schematic diagram of eddy-induced horizontal advection of SST for clockwise and counterclockwise-rotating eddies (top and bottom, respectively) propagating westward in regions where the SST gradient is (a) southward and (b) southwestward. An otherwise smooth contour of SST (dashed lines) is distorted by the rotational velocity field within the eddy, as shown by the solid lines. Advection of SST within the large-scale background SST gradient results in the positive and negative SST anomalies shown by the red and blue regions, respectively. The dependence of the locations of these SST anomalies on the direction of the large-scale background SST gradient that is evident from comparison of (a) and (b) was accounted for by compositing eddy-induced anomalies of SST in a coordinate system rotated in the direction of the background large-scale SST field for each eddy.

all midlatitude eddies in a northward gradient in Fig. 3b are in the Southern Hemisphere.

An important distinction between the eddy-induced SST anomalies in Figs. 3a and 3b and the observed near-surface chlorophyll anomalies (CHL) and modeled tracer anomalies reported by Chelton et al. (2011a) is that the asymmetry of the dipoles of the SST composites is greater than that observed in the CHL and model tracer composites. This asymmetry is measured by the ratio of the magnitudes of the primary pole in the western half of the composites to the magnitude of the secondary pole in the eastern half of the composites, denoted by  $r$  in Fig. 3. Values of  $r$  for the SST anomaly composites range between  $\sim 2.1$  and  $2.7$ . In contrast,  $r \sim 1.3$ – $1.7$  for observed CHL and modeled passive tracer (Chelton et al. 2011a).

The stronger asymmetry of the dipole structure in SST is consistent with an interpretation of the eddy-induced SST anomalies as a superposition of a monopole core of cold (warm) water from upwelling (downwelling) centered on the eddy interior and a dipole SST structure with the asymmetry of CHL documented by Chelton et al. (2011a). For example, superimposing a scaled version of a moderately asymmetric dipole with a typical

asymmetry ratio of  $r = 1.5$  with an axisymmetric Gaussian-shaped SST monopole anomaly with a representative extremum of  $0.3^\circ\text{C}$  gives an asymmetry ratio of  $r = 2.7$ , which is very similar to the midlatitude SST composite average shown in the right panel of Fig. 3b. As the eddy amplitude increases, and hence the rotational velocity and nonlinearity of the eddy increase, the eddy-induced SST structure converges toward a monopole structure centered close to the eddy SSH extremum (Fig. 4). Consistent with this interpretation, composites from the 8783 eddy realizations in the upper 5th percentile of amplitude have nearly monopolar SST anomalies, with ratios  $r = 5.0$  for anticyclones and  $4.7$  for cyclones (Fig. 4c).

Wind speed is expected to respond approximately linearly to mesoscale eddy-induced SST anomalies in accordance with previous studies of air–sea interaction over SST frontal regions (e.g., O’Neill et al. 2012). Wind speed anomalies composited in the same rotated coordinate system as the SST composites (Figs. 3c,d) have the same structure as the SST composites in Figs. 3a and 3b. This close relationship between SST and the relative surface winds is expected from the previous studies of mesoscale air–sea interaction summarized in the introduction. A



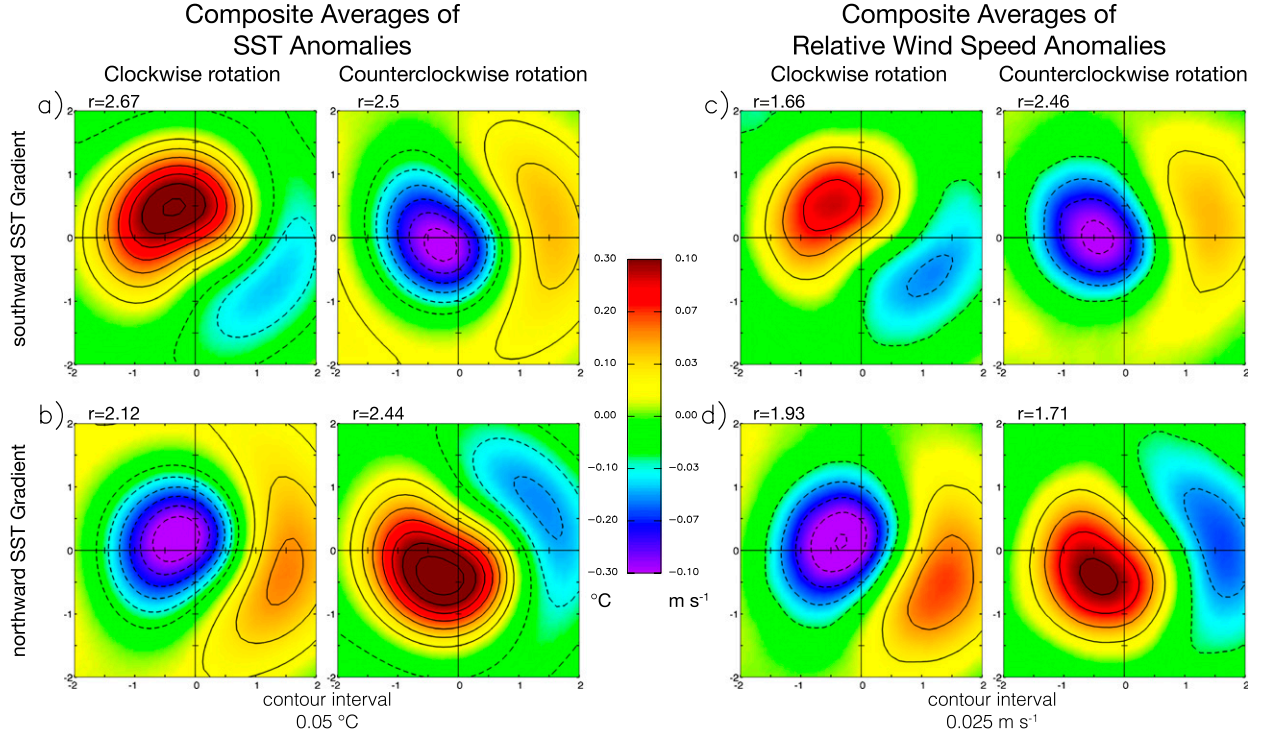


FIG. 3. Composite averages of anomalies of (a),(b) SST and (c),(d) wind speed in midlatitude eddies. Eddies are segregated according to the meridional direction of the background SST gradient, either southward or northward, and the rotational sense of the eddies, either clockwise or counterclockwise. The composite averages were constructed by rotating the coordinate system for each eddy realization to align the background SST gradient to a polar angle of either  $\pm 90^\circ$ . The magnitude of the asymmetry between the primary and secondary poles of the anomalies is labeled as the value  $r$  in each panel. The  $x$  and  $y$  coordinates of the composite averages are normalized by the eddy radius scale  $L_s$ , defined in section b. The contour intervals of the SST and wind speed composites are  $0.05^\circ\text{C}$  and  $0.025\text{ m s}^{-1}$ , respectively.

coupling coefficient  $\alpha_{\text{SST}}^{\text{spd}} = 0.28\text{ m s}^{-1}\text{ }^\circ\text{C}^{-1}$  was estimated in eddy interiors by least squares regression of the relative wind speed perturbations, bin averaged on the collocated SST anomalies for all midlatitude eddies with lifetimes of 12 weeks and longer. This falls within the  $0.2\text{--}0.6\text{ m s}^{-1}\text{ }^\circ\text{C}^{-1}$  geographical range of coupling coefficients previously reported for various SST frontal regions (O'Neill et al. 2010; O'Neill 2012; O'Neill et al. 2012) and the regions investigated in section 6 (Table 2). It is thus seen that the air–sea interaction studied extensively in SST frontal regions also occurs over eddy-induced SST anomalies. Motivated by this analysis, and the relationship between the relative wind  $\mathbf{u}_{\text{rel}}$  and surface stress  $\boldsymbol{\tau}$  in (2), anomalies of the surface stress curl induced by eddy SST anomalies are computed for the eddy composites of  $W_{\text{SST}}$  in the following sections and compared with the Ekman pumping effects induced by eddy surface currents.

#### 4. Eddy-induced Ekman pumping in idealized eddies

The effects of the SST-induced and surface current-induced Ekman pumping for idealized but realistic

eddies are examined in this section in order to assess their relative importance. To estimate the magnitude of the SST-induced Ekman pumping  $W_{\text{SST}}$ , we consider idealized eddy-induced SST anomalies with the structure of the composites shown in Fig. 3a, scaled to have a realistic maximum amplitude of  $0.3^\circ\text{C}$ . The SST-induced surface stress curl associated with the idealized SST anomalies was computed using a constant coupling coefficient  $\alpha_c^{\text{strecrl}} = 0.013\text{ N m}^{-2}\text{ }^\circ\text{C}^{-1}$  in (4), representative of the average coupling coefficient in midlatitude eddies (Table 2).

To estimate the effects of eddy surface velocity on current-induced Ekman pumping  $W_{\text{cur}}$ , we consider a Gaussian eddy at  $30^\circ\text{N}$  with SSH defined as

$$\eta(r) = A \exp\left(-\frac{1}{2}b^2r^2\right), \quad (13)$$

where  $A$  is the amplitude,  $r = \sqrt{(x - x_o)^2 + (y - y_o)^2}/L_s$  is the radial distance from the eddy SSH extremum located at  $x = x_o$  and  $y = y_o$  normalized by the speed-based radius scale  $L_s$ , and  $b = L_s/L$  is the dimensionless ratio of the speed-based radius scale  $L_s$  to the Gaussian

# Rotated Composite Average SST Anomalies Northward Ambient SST Gradient

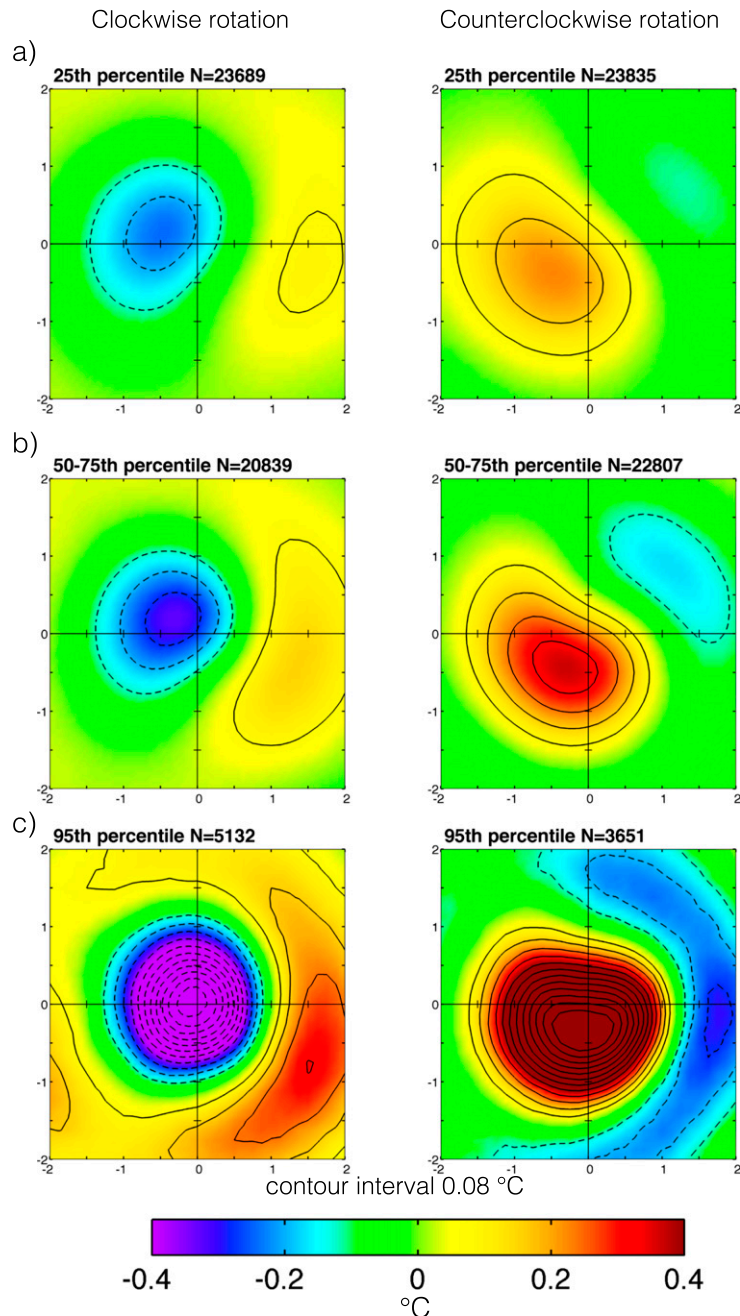


FIG. 4. Composite-averaged SST anomalies for eddies in a northward ambient SST gradient. As in Fig. 3, each individual weekly eddy observation is rotated to align the ambient SST gradient to a polar angle of  $90^\circ$  and is normalized by the horizontal eddy scale  $L_s$  before averages are computed. Composites are segregated by the SSH amplitude of each eddy realization with (left) clockwise- and (right) counterclockwise-rotating eddies. The panel pairs correspond to eddies with (a) amplitudes  $\leq 3.1$  cm, representative of the 25th percentile of long-lived midlatitude eddies, (b) amplitudes  $> 5.2$  cm and  $\leq 8.9$  cm (50th to 75th percentile), and (c) amplitudes  $\geq 22.5$  cm (the upper 5th percentile of eddy amplitude). The contour interval is  $0.08^\circ\text{C}$  and the number of eddy realizations used in each of the composites is labeled as  $N$  in the title of each panel.

eddy radius scale  $L$  (equal to the radius of maximum rotational speed for an axisymmetric Gaussian eddy).

For the present purpose of evaluating surface current contributions to eddy-induced Ekman pumping, we chose a combination of Gaussian eddy amplitude  $A = 14.5$  cm and the nondimensional parameter  $b = 1.2$  to fit the observed composite-averaged geostrophic current velocity profile of midlatitude anticyclonic eddies (cf. thin and thick lines in Figs. 5b). For the global mean observed value of  $L_s = 90$  km, this yields a Gaussian eddy radius scale  $L = L_s/b = 75$  km. Although this choice of  $A$  and  $b$  resulted in a very good approximation of the global composite average geostrophic current speed, the global composite-averaged SSH and geostrophic current vorticity magnitude are slightly overestimated (Figs. 5a,c).

*a. SST-induced Ekman pumping for an idealized eddy-induced SST anomaly*

For a  $7 \text{ m s}^{-1}$  westerly background wind over Northern Hemisphere anticyclones and cyclones, the SST-induced Ekman pumping velocities are approximately  $4 \text{ cm day}^{-1}$  (rows 1 and 3 of Fig. 6a). The structure of SST-induced Ekman pumping  $W_{\text{SST}}$  depends strongly on the direction of the background wind;  $W_{\text{SST}}$  for uniform westerly and poleward winds are rotated  $90^\circ$  relative to each other and are somewhat different in structure and magnitude (Fig. 6a). These differences arise from asymmetries in the SST structure and the associated crosswind SST gradient. As shown in Fig. 7a, the magnitude of  $W_{\text{SST}}$  varies linearly with the magnitude of the SST anomalies and is generally  $< 7 \text{ cm day}^{-1}$  for the coupling coefficient used for this estimate of  $W_{\text{SST}}$  for idealized but realistic eddies. The structure of  $W_{\text{SST}}$  for Southern Hemisphere eddies similarly depends on the structure of the eddy-induced SST anomalies and the direction of the background wind. In the Southern Hemisphere, the sign of SST-induced Ekman pumping for a given SST anomaly is opposite that in the Northern Hemisphere as a result of the dependence of  $W_{\text{SST}}$  on  $1/f$  in (8).

*b. Surface current-induced Ekman pumping for an idealized Gaussian eddy*

The magnitudes of  $W_c$  exceed  $12 \text{ cm day}^{-1}$  for a  $7 \text{ m s}^{-1}$  background wind (Fig. 6b). Minor side lobes of weak Ekman pumping of opposite sign occur on the flanks of the eddies, aligned laterally with the wind direction. When the same axisymmetric Gaussian eddies are exposed to a longitudinally uniform poleward wind, the spatial structure and magnitude of the resulting  $W_c$  are identical to those of the westerly wind case, except rotated in accordance with the wind direction (cf. rows 1 and 3 with rows 2 and 4 in Fig. 6b). Because the direction

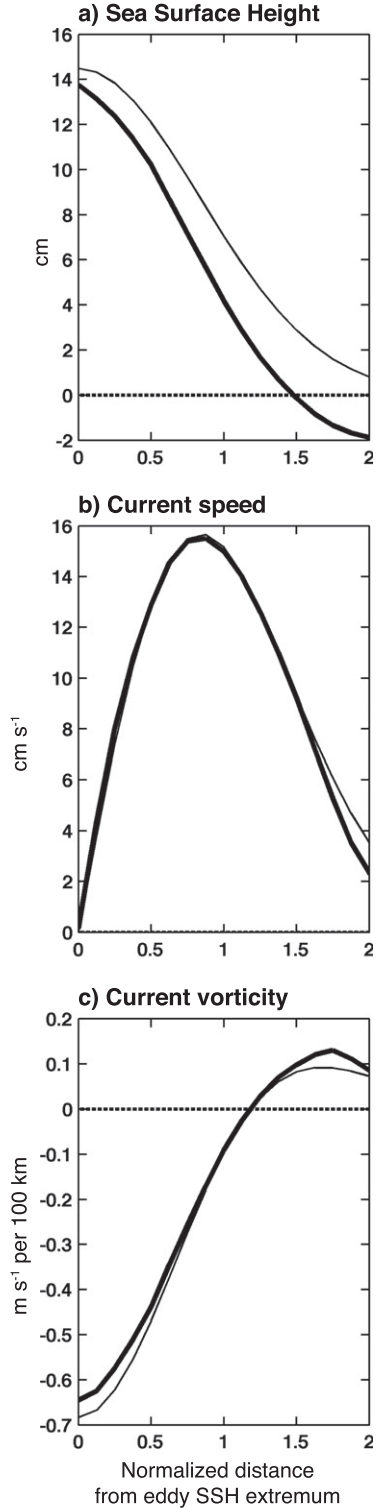


FIG. 5. Azimuthal averages of composite-averaged (a) SSH, (b) geostrophic current speed, and (c) geostrophic current vorticity for midlatitude anticyclones (thick curve) and a Gaussian SSH structure given by (13) with amplitude  $A = 14.5$  cm and parameter  $b = 1.2$  (thin curve). The  $x$  axis in all panels has been normalized by the speed-based radius scale  $L_s$ , which has the global mean value  $L_s = 90$  km.



# Ekman Pumping in Idealized Northern Hemisphere Eddies

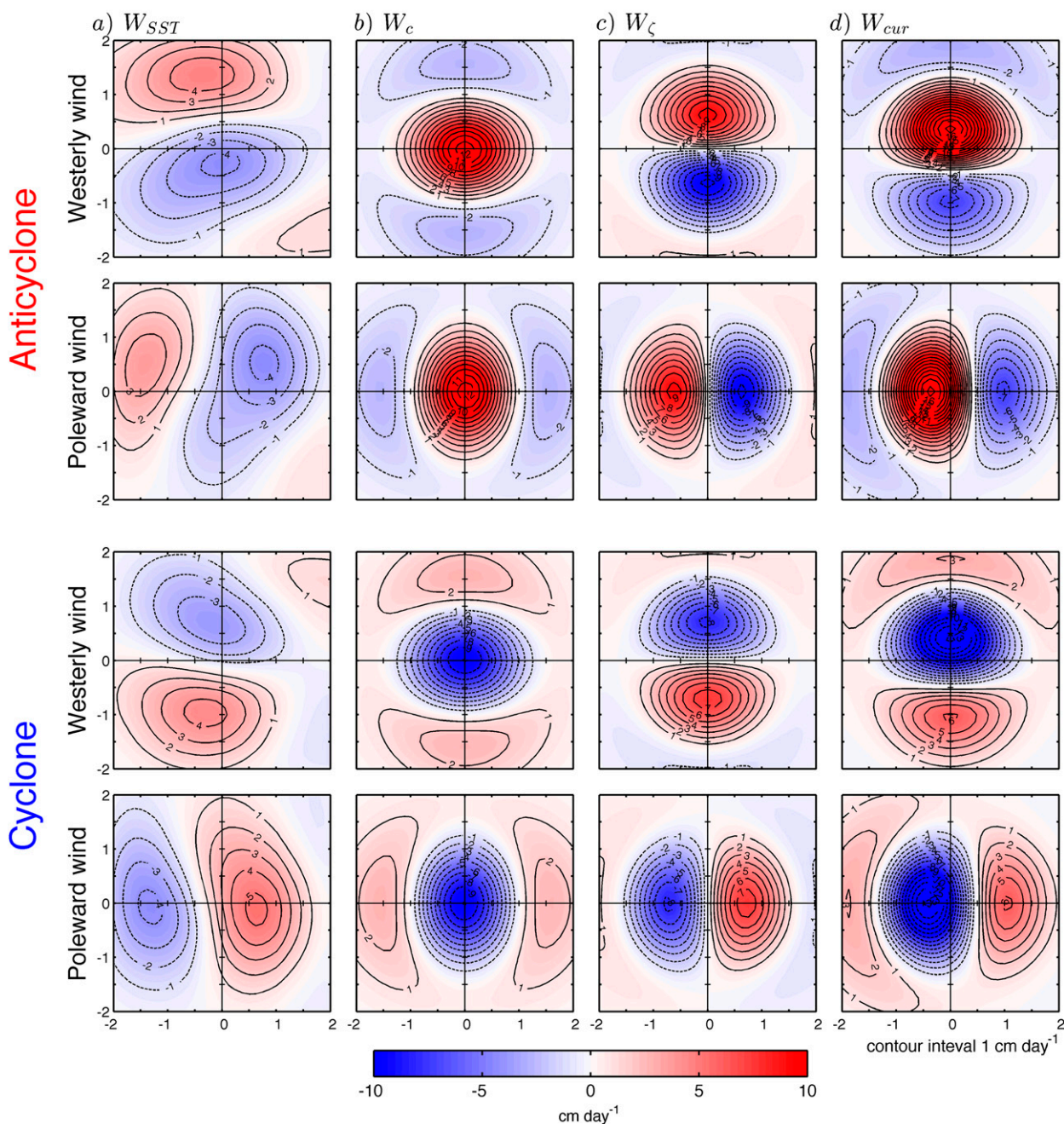


FIG. 6. The geographical structure of the various contributions to total eddy-induced Ekman pumping from the idealized (top) anticyclone and (bottom) cyclone with SST shown in Fig. 3a and SSH shown in Fig. 5a, rotating under uniform  $7 \text{ m s}^{-1}$  westerly (rows 1 and 3) and poleward (rows 2 and 4) winds. (a) SST-induced Ekman pumping  $W_{SST}$ , (b) surface stress curl-induced Ekman pumping  $W_c$ , (c) current vorticity gradient-induced Ekman pumping  $W_\zeta$ , and (d) the total current-induced Ekman pumping  $W_{cur}$ , defined as the sum of (b) and (c). The x and y axes have been normalized by  $L_s$ , which corresponds to the radius of maximum rotational speed for a Gaussian eddy.

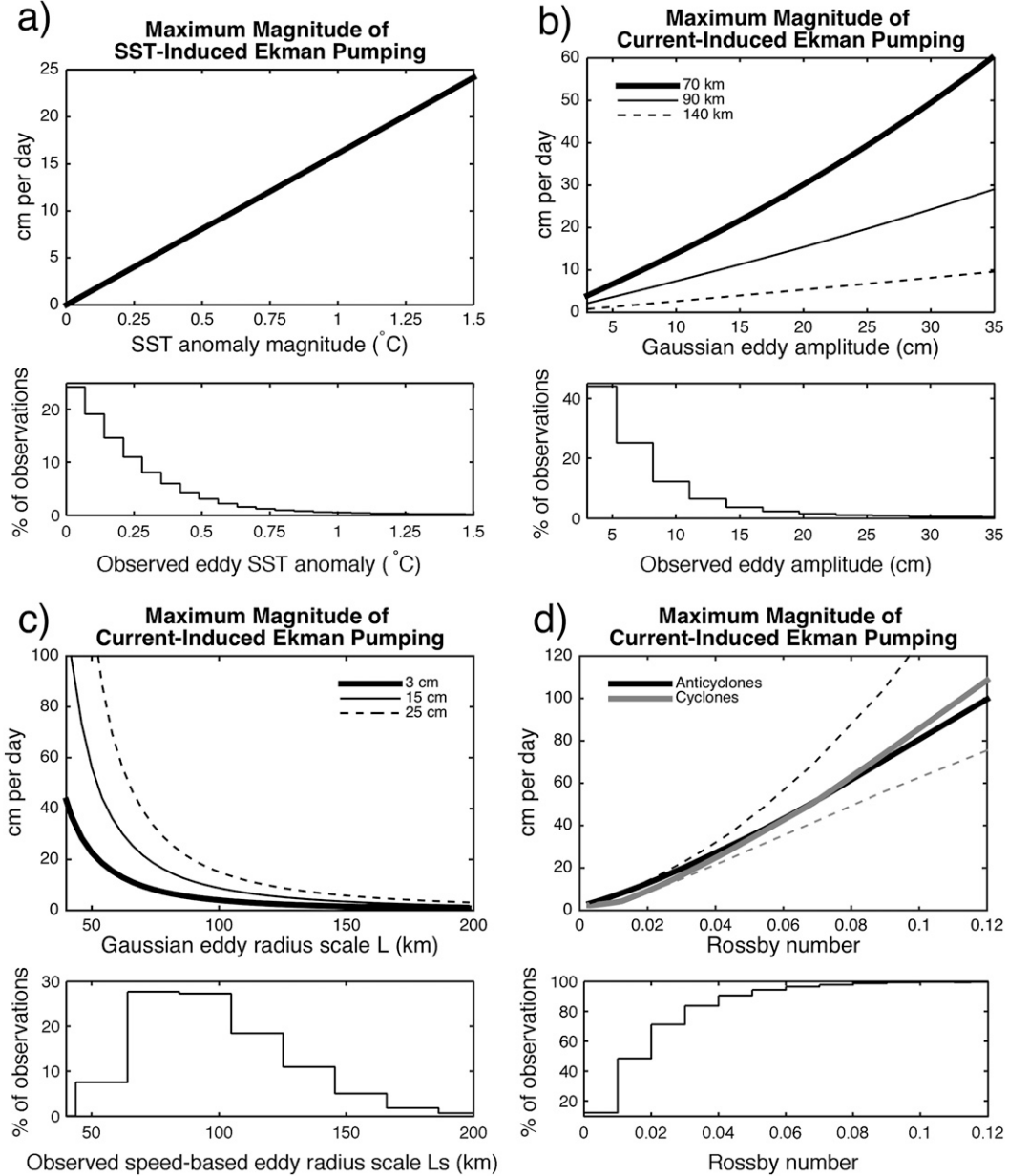


FIG. 7. (a) The maximum magnitude of SST-induced Ekman pumping  $W_{\text{SST}}$  [(8)] for an idealized SST anomaly like the left panel of Fig. 5a as a function of the magnitude of the SST anomaly (upper panel) and the histogram of the observed eddy SST anomalies within the interiors of mesoscale eddies (lower panel). (b) The maximum magnitude of total current-induced Ekman pumping  $W_{\text{cur}}$  [(10)] as a function of eddy amplitude for Gaussian eddies with radial scales of 70, 90, and 140 km, corresponding to the 25th, 50th, and 95th percentiles of midlatitude speed-based eddy scale  $L_s$  (upper panel) and the histogram of observed midlatitude eddy amplitudes (lower panel). (c) The maximum magnitude of  $W_{\text{cur}}$  as a function of eddy radius scales for Gaussian eddies amplitudes of 3, 15, and 25 cm, corresponding to the 25th, 50th, and 95th percentiles of midlatitude eddy amplitudes (upper panel) and the histogram of observed speed-based eddy radius scales  $L_s$  (lower panel). (d) Maximum magnitude of current-induced Ekman pumping (upper panel) for idealized eddies with Gaussian structure with fixed amplitude of 10 cm and radius scales ranging from 30 to 200 km. The variable  $L_s$  results in a range of Rossby numbers, defined as  $\text{Ro} = \zeta/f$ , where  $\zeta$  is the relative vorticity of the eddy and  $f$  is the Coriolis parameter. Anticyclones and cyclones shown as black and gray curves, respectively. Thick solid curves represent the total eddy-induced Ekman pumping computed assuming that the geostrophic current vorticity  $\zeta$  is small compared to  $f$  ( $\text{Ro}$  is small), and thin dashed curves represent the total eddy-induced Ekman pumping computed including  $\zeta$  in the denominator. The cumulative histograms of observed Rossby numbers are shown in the lower panel.



of rotation for a given eddy polarity and the Coriolis parameter  $f$  both have opposite sign in the Northern and Southern Hemispheres, the spatial structures of  $W_c$  in the Southern Hemisphere are identical to those shown in Fig. 6b.

The contribution  $W_\zeta$  [(7)] from surface current vorticity gradient-induced Ekman pumping has antisymmetric dipoles of upwelling and downwelling with slight asymmetry of the magnitudes of the two poles and with signs and orientation dictated by the sign of the relative vorticity gradient and the direction of the background wind (Fig. 6c). The antisymmetry arises from the eddy surface current influence on the relative wind and hence on the surface stress. The surface stress is enhanced over regions of the eddy where the absolute wind blows against the rotating eddy surface currents. Because  $W_\zeta$  depends on  $\nabla\zeta/(f + \zeta)^2$ , the signs of the dipoles of  $W_\zeta$  are reversed in the Southern Hemisphere relative to Fig. 6c.

The total current-induced Ekman pumping  $W_{\text{cur}} = W_c + W_\zeta$  has upwelling in the cores of anticyclones and downwelling in the cores of cyclones, centered about  $0.5L_s$  to the left of the eddy SSH extremum when facing in the downwind direction in the Northern Hemisphere (Fig. 6d). The primary pole of  $W_{\text{cur}}$  is located to the right of the wind in the Southern Hemisphere. A relatively weak secondary pole of Ekman pumping of the opposite sign occurs to the right of the wind direction in the Northern Hemisphere and to the left in the Southern Hemisphere. The maximum pumping velocity from  $W_{\text{cur}}$  for the idealized but realistic eddy considered here is  $\sim 14 \text{ cm day}^{-1}$  and is centered to the north of the eddy SSH extremum under an eastward wind and to the west under a northward wind in the Northern Hemisphere. The maximum magnitude of  $W_{\text{cur}}$  increases with eddy amplitude for Gaussian eddies with a given radius (Fig. 7b) and decreases with eddy radius for a given amplitude (Fig. 7c).

Since  $W_c$  has a polarity opposite that of the eddy, it generates upwelling (downwelling) in the cores of anticyclones (cyclones), as noted by Dewar and Flierl (1987). For the mesoscale eddies of interest here,  $W_{\text{cur}}$  (Fig. 6d) has a pattern qualitatively similar to  $W_c$ . As a result of the combination of the monopole of  $W_c$  with the dipole of  $W_\zeta$ , the extremum is displaced from the center of the eddy and there is a second extremum with opposite sign, resulting in a dipole structure with very asymmetric amplitudes of the two poles. The primary pole of strong  $W_{\text{cur}}$  within the eddy cores is somewhat elongated parallel to the wind direction (Fig. 6d). Likewise, the weaker secondary pole of  $W_{\text{cur}}$  with sign opposite that of the primary pole is also elongated parallel to the wind direction. These elongations arise from the nonlinear relation between the stress and the relative wind.

Global and regional composite averages constructed from observed eddies are presented in sections 5 and 6, respectively, and compared qualitatively with the Ekman pumping patterns in Fig. 6 for the idealized eddies in uniform, constant winds. The degree to which composite averages of  $W_{\text{cur}}$  in a geographically fixed coordinate system over many realizations retain the dipolar structures in Fig. 6d depends on how variable the wind direction is. The blurring from variable wind direction can be mitigated by composite averaging in a rotated coordinate system defined by the background wind direction (see section 5). Since the magnitude of  $W_{\text{cur}}$  depends on the ambient wind speed, composite averages will also depend on the variability of the wind speed.

For the characteristic midlatitude eddies considered for the idealized calculations in Fig. 6,  $W_{\text{SST}}$  is generally much smaller in magnitude than  $W_{\text{cur}}$ . From the consideration of regional variability in section 6, however, it is shown that the  $W_{\text{SST}}$  influence on Ekman pumping can approach, and even exceed,  $W_{\text{cur}}$  in regions of intense SST gradients.

The spatial structures of the two dominant contributions to Ekman pumping ( $W_c$  and  $W_\zeta$ ) result in very different net vertical displacements of water parcels circulating within the eddy core. From a Lagrangian perspective, the net vertical displacement of a parcel of water as it travels in a circuit around the eddy center can be estimated from the azimuthal averages of each contribution to Ekman pumping around geostrophic streamlines (approximately equal to contours of SSH). This net vertical displacement is dominated by  $W_c$ , while  $W_\zeta$  averages to very small values (McGillicuddy et al. 2008). For nutrients or phytoplankton circulating within an eddy interior, it is thus apparent that net vertical displacement is controlled predominately by  $W_c$ . In light of this and the fact that their interest was in eddy influence on the biology, Martin and Richards (2001), McGillicuddy et al. (2007, 2008), and Gaube et al. (2013) approximated  $W_{\text{cur}}$  by  $W_c$ . In the present study, however, our interest is in the total Ekman pumping from an Eulerian point of view. As such, the contribution  $W_\zeta$  cannot be neglected.

## 5. Observed eddy-induced Ekman pumping at midlatitudes

To investigate the relative contributions of SST and surface current effects in the global midlatitude mean, we consider the total estimated Ekman pumping  $\tilde{W}_{\text{tot}}$  [(5)] as the sum of the current-induced Ekman pumping [(10)] and the SST-induced Ekman pumping [(8)] and compare composite averages of  $\tilde{W}_{\text{tot}}$  to composite averages of  $W_{\text{tot}}$  computed from QuikSCAT wind observations.

Because of the dependence of eddy-induced Ekman pumping on wind direction (section 4b), the composites

of midlatitude eddies investigated here are constructed in two different coordinate systems: a rotated coordinate system that aligns the large-scale background wind direction to a polar angle of  $0^\circ$  (this corresponds to no coordinate rotation for eddies in a westerly wind field) and in an unrotated, north–south/east–west coordinate system. The wind direction was computed for each individual eddy realization as the average large-scale background wind direction, defined by  $6^\circ \times 6^\circ$  smoothing of the vector wind components, in a  $4^\circ \times 4^\circ$  box centered on the eddy SSH extremum.

Rotated composite averages of  $W_{\text{tot}}$  (left panels of Figs. 8a and 9a) are very similar to  $\tilde{W}_{\text{tot}}$  (left panels of Figs. 8b and 9b), except with slightly larger magnitudes. The difference in magnitude is likely a result of QuikSCAT resolving smaller spatial scales than are resolved in the optimally interpolated SSH field from which  $\tilde{W}_{\text{tot}}$  is estimated and possibly because of underestimation of SST gradients caused by resolution limitations of the SST dataset used here (Reynolds and Chelton 2010). Regardless of the small difference in the magnitudes of  $W_{\text{tot}}$  and  $\tilde{W}_{\text{tot}}$ , the close similarities between  $W_{\text{cur}}$  and  $W_{\text{tot}}$  clearly indicate that  $W_{\text{tot}}$  in midlatitude eddies is predominantly controlled by  $W_{\text{cur}}$ , consistent with the conclusions in section 4 that  $W_{\text{SST}}$  is generally small compared to  $W_{\text{cur}}$  (see Figs. 6, 7a–c).

Composite averages of the different components of eddy-induced Ekman pumping for Northern Hemisphere midlatitude eddies constructed in the rotated coordinate system (left two panels of Figs. 8c,d) are very similar to the Ekman pumping signatures of idealized Northern Hemisphere eddies under westerly winds considered in section 4b (first and third panels of Figs. 6a,d). The rotated composite averages recover the elongated primary and secondary poles of  $W_{\text{cur}}$  (the left two panels of Figs. 8c,d).

The importance of constructing composite averages in the rotated coordinate system to see the relation to the idealized calculations in section 4b becomes apparent when comparing the rotated composites (left two panels of Figs. 8, 9) to the unrotated composites (right two panels of Figs. 8, 9); the asymmetric dipoles of  $W_{\text{cur}}$  expected from the idealized eddies considered in section 4 are lost when composite averaging in a fixed geographical coordinate system because of variations in wind direction and, to a lesser extent, wind speed.

Northern Hemisphere rotated composite averages of  $W_{\text{SST}}$  in anticyclones (cyclones) are dipolar, with upwelling (downwelling) and downwelling (upwelling) centered to the rotated equivalent north and south of the composite-averaged eddy SSH extremum, respectively (left two panels of Fig. 8d). Rotated composite averages of  $W_{\text{SST}}$  in Southern Hemisphere eddies consist of similar dipoles, but with opposite signs (left two panels of

Figs. 9d). The primary poles of  $W_{\text{cur}}$  in the rotated composites have maximum Ekman pumping velocities of  $\sim 10 \text{ cm day}^{-1}$  (left two panels of Figs. 8c, 9c), which is 4–5 times larger than  $W_{\text{SST}}$  in these hemispheric composites. This is consistent with the conclusions in section 4 for the idealized eddies.

The geographical variations of the magnitudes  $|W_{\text{cur}}|$  and  $|W_{\text{SST}}|$  are shown in Fig. 10. Because of their dependence on the Coriolis parameter  $f$  [see (6)–(8) and (10)],  $W_{\text{cur}}$  and  $W_{\text{SST}}$  increase toward the equator. To compare their geographical variability, it is thus convenient to normalize by the multiplicative factor  $f/f_o$  where  $f_o = f(30^\circ)$ . In the midlatitudes,  $|fW_{\text{cur}}/f_o|$  is highest in regions of energetic mesoscale eddies (Fig. 10a), such as near boundary currents where eddy amplitudes are large (see Fig. 10 of Chelton et al. 2011b), and at high southern latitudes where the radial scales of eddies are small compared with those at lower latitudes (see Fig. 12 of Chelton et al. 2011b).

In regions of large ambient SST gradients, such as in the midlatitude extensions of the major western boundary currents and the Antarctic Circumpolar Current, lateral variations of wind speed across SST fronts can generate  $|W_{\text{SST}}|$  that is comparable to, and sometimes larger than,  $|W_{\text{cur}}|$  (Figs. 10b,c). The ratio of the average magnitude of  $W_{\text{SST}}$  to  $W_{\text{cur}}$  in Fig. 10c also suggests that  $|W_{\text{SST}}|$  can be greater than  $|W_{\text{cur}}|$  in central gyre regions, such as in the North and South Pacific and the South Atlantic, that are populated by small-amplitude eddies (cf. Fig. 10c with Fig. 10 of Chelton et al. 2011b). This is misleading, however, since the global map of normalized  $|W_{\text{SST}}|$  in Fig. 10c was computed using a fixed coupling coefficient of  $\alpha_c^{\text{strcr1}} = 0.013 \text{ N m}^{-2} \text{ }^\circ\text{C}^{-1}$ , representative of the global average (Table 2), which is much larger than is observed in the central gyre regions investigated in sections 6c–e (Table 2). This likely results in an overestimation of  $W_{\text{SST}}$  in central gyre regions. This is confirmed in the regional analyses in sections 6c–e, which utilize  $\alpha_c^{\text{strcr1}}$  specific to each region, and also by computing a global map of  $W_{\text{SST}}$  using spatially variable  $\alpha_c^{\text{strcr1}}$ , which results in  $W_{\text{SST}}$  that is much smaller than  $W_{\text{cur}}$  in these gyre regions (not shown here). Even in light of the overestimation of  $W_{\text{SST}}$  in Fig. 10c,  $W_{\text{SST}} < W_{\text{cur}}$  over 79% of the ocean’s surface (Fig. 10d).

## 6. Regional variability of eddy-induced Ekman pumping

### a. Regions and compositing

The global composites in Figs. 8 and 9 provide a useful comparison of observed eddy-induced Ekman pumping with the idealized cases of section 4. However, both the

# Northern Hemisphere Composite Averages

Rotated

Not Rotated

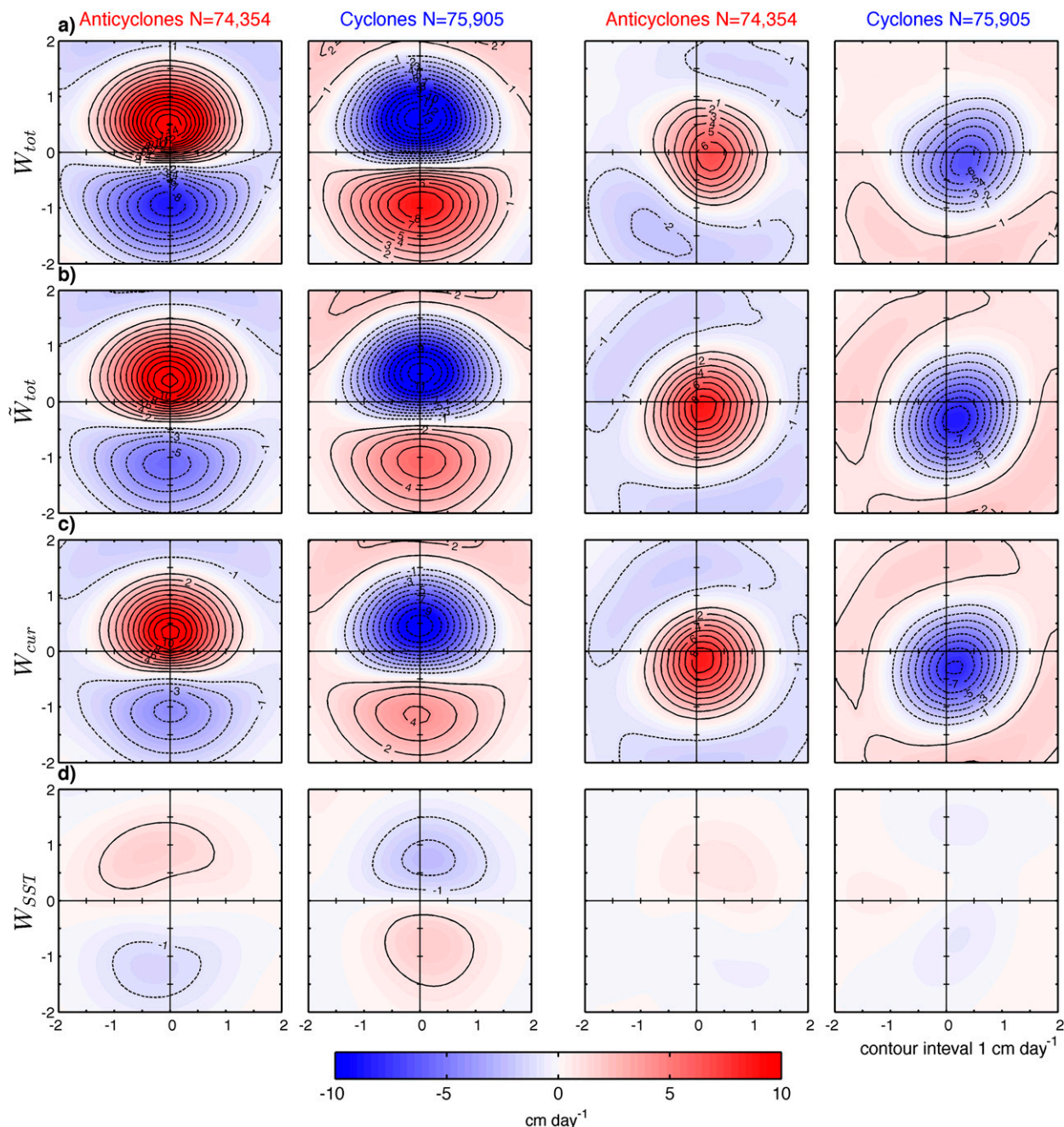


FIG. 8. Composite averages of eddy-induced Ekman pumping in Northern Hemisphere midlatitude eddies ( $15^{\circ}$ – $45^{\circ}$ N latitude) constructed separately for anticyclones and cyclones, and in (left two columns) a rotated coordinate system that aligns the smoothed background wind direction to a polar angle of  $0^{\circ}$  and (right two columns) an unrotated, Cartesian coordinate system. (a) Observed total eddy-induced Ekman pumping computed  $W_{\text{tot}}$  from the QuikSCAT surface stress curl. (b) The sum of (c) the total current-induced Ekman pumping  $W_{\text{cur}}$  and (d) the SST-induced Ekman pumping  $W_{\text{SST}}$ , computed using a constant coupling coefficient of  $\alpha_c^{\text{strcl}} = 0.013 \text{ N m}^{-2} \text{ }^{\circ}\text{C}^{-1}$  (Table 2). The  $x$  and  $y$  coordinates of the composite averages are normalized by the eddy scale  $L_s$ . The number of individual eddy realizations is labeled as  $N$  at the top of each column.



# Southern Hemisphere Composite Averages

Rotated

Not Rotated

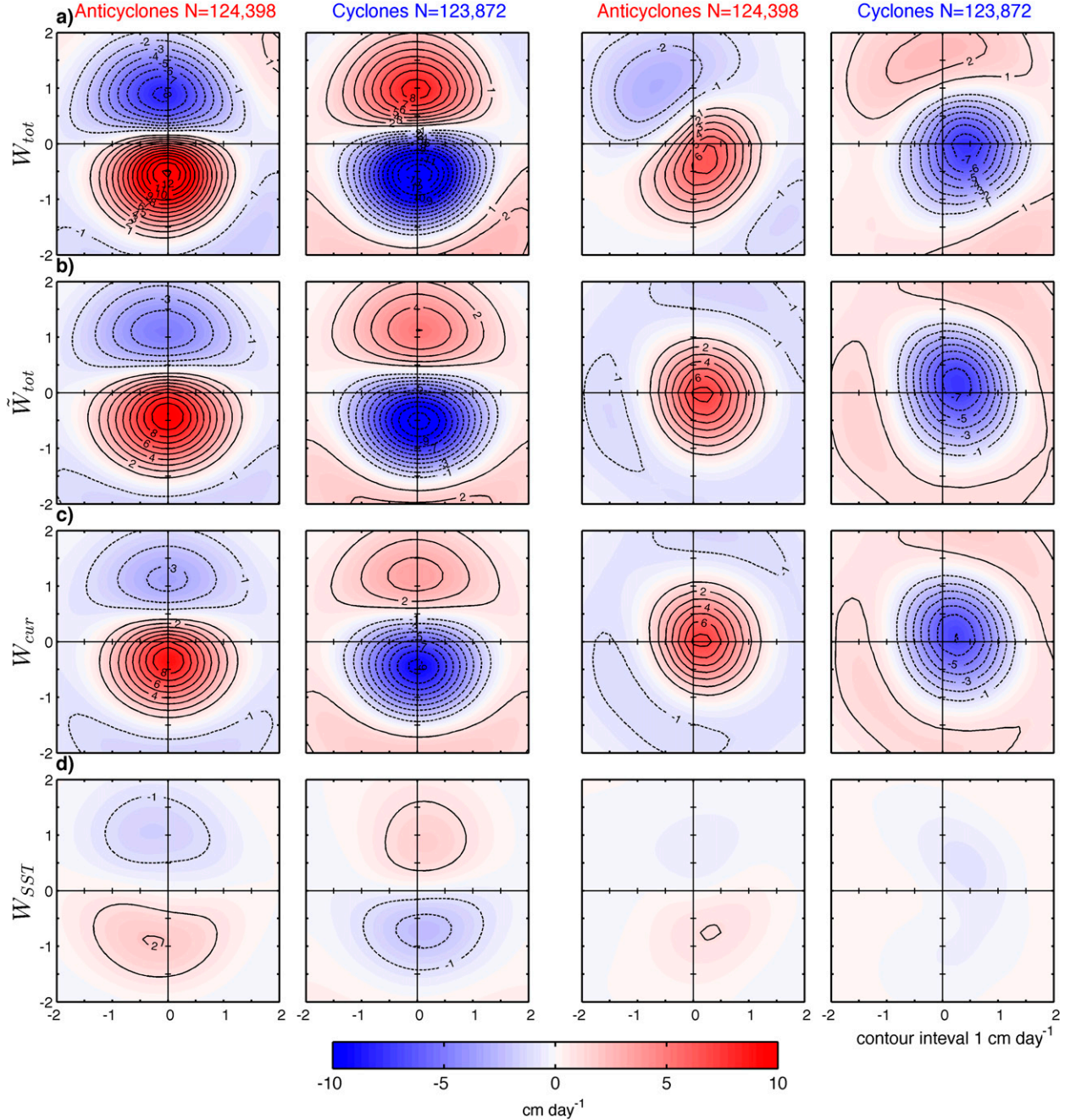


FIG. 9. As in Fig. 8, but for eddies in the latitude range 15°–45°S.

relative importance of  $W_{cur}$  and  $W_{SST}$  and the strength of the air–sea interaction embodied in the coupling coefficient  $\alpha_c^{\text{strcrf}}$  in (12) vary regionally (Table 2). To examine how eddy-induced Ekman pumping varies regionally, this section presents an analysis for six

diverse regions of the World Ocean (Fig. 11). The Agulhas Return Current and southeast Atlantic (SEA) regions were chosen because of a historical precedent for studies of air–sea interaction over SST fronts in these regions (e.g., O’Neill et al. 2005, 2012). The Caribbean

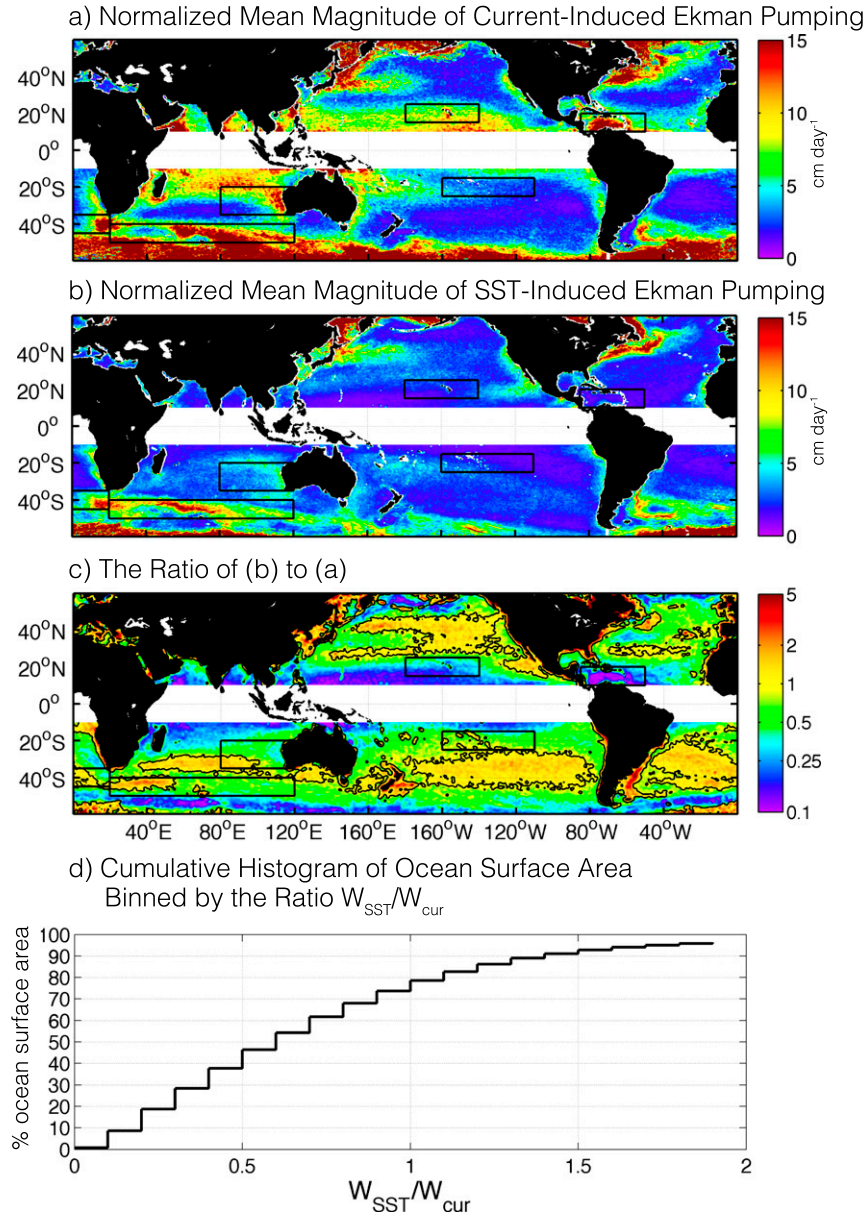


FIG. 10. Global  $1/4^\circ \times 1/4^\circ$  maps of averages over the 7.5-yr data record of (a)  $\langle |W_{cur}| \rangle (f/f_o)$  and (b)  $\langle |W_{SST}| \rangle (f/f_o)$ , where  $\langle \rangle$  indicates time averages,  $f_o = f(30^\circ)$ , and the multiplicative factor  $(f/f_o)$  removes the strong latitudinal dependence of Ekman pumping on  $1/f$ . The averages shown in (a) and (b) are masked to only include observations within the interiors of mesoscale eddies.  $W_{SST}$  was computed using a fixed coupling coefficient of  $\alpha_c^{strcl} = 0.013 \text{ N m}^{-2} \text{ } ^\circ\text{C}^{-1}$ . (c) The ratio of (b) to (a), plotted on a log scale. The black contours correspond to a smoothed ratio of 1. (d) Cumulative histogram of the ocean's surface area binned by the ratio in (c).

Sea and the central Pacific around the Hawaiian Islands were chosen because they are regions of strong current-induced Ekman pumping (Fig. 10a), relatively steady winds (Fig. 12), and weak background SST gradients. The south Indian Ocean (SIO) and the South Pacific Ocean were chosen because of the potential role that  $W_{tot}$  can have on ecosystems trapped within the eddy

cores in these oligotrophic (low nutrient) regions (Gaube 2012; Gaube et al. 2013, 2014).

Composite averages were computed from each region in a fixed geographical coordinate system. For these six regions, composite averages constructed in a rotated coordinate system aligned with the wind are very similar to the unrotated composites, except slightly larger in



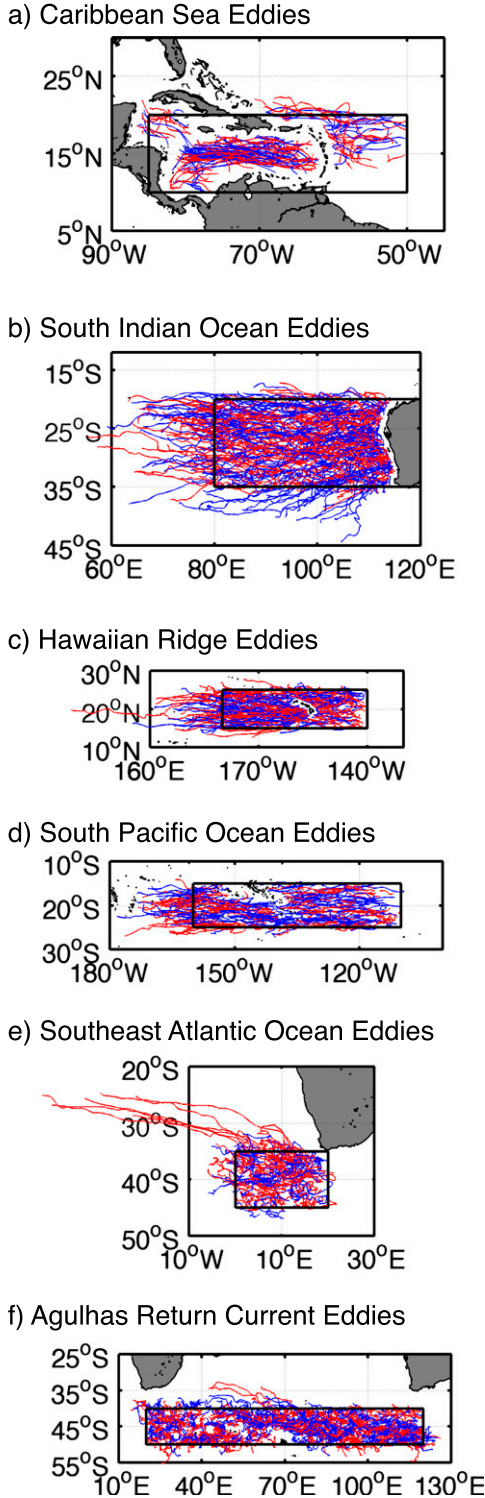


FIG. 11. Trajectories of the long-lived mesoscale eddies (lifetimes  $\geq 12$  weeks) used to construct the composites shown in Figs. 13 through 18. Anticyclones are shown in red and cyclones in blue: (a) CAR, (b) SIO, (c) HAW, (d) SPO, (e) SEA, and (f) ARC. The eddy trajectories were smoothed with a half span of 6 weeks prior to plotting.

magnitude and rotated in orientation in accordance with the direction of the background wind (not shown here). The similarity of the rotated and unrotated regional composites is a result of the direction of the wind being fairly steady within each region (Fig. 12). The wind stress curl coupling coefficient  $\alpha_c^{\text{strcr1}}$  was computed individually for each of the six regions (Table 2). The trajectories of the eddies in the six regions are shown in Fig. 11.

*b. The Caribbean Sea ( $10^\circ$ – $20^\circ$ N,  $275^\circ$ – $310^\circ$ E)*

The Caribbean Sea is characterized by steady easterly trade winds (Fig. 12). The trajectories of CAR eddies are shown in Fig. 11a, and the statistics of the eddies are summarized in Fig. 1a and Table 1. Both  $W_{\text{SST}}$  and  $W_{\text{cur}}$  have a qualitatively similar dipolar structure, but the small SST anomalies of CAR eddies (Fig. 13b) generate  $W_{\text{SST}}$  that is an order of magnitude smaller than  $W_{\text{cur}}$  (Figs. 10a,b), and it thus has a negligible effect on  $\bar{W}_{\text{tot}}$  in Fig. 13f. The total eddy-induced Ekman pumping  $\bar{W}_{\text{tot}}$  derived from QuikSCAT (Fig. 13c) is very similar to  $W_{\text{cur}}$  and  $\bar{W}_{\text{tot}}$  (Figs. 13d,f). The maximum Ekman pumping velocities of both  $W_{\text{tot}}$  and  $\bar{W}_{\text{tot}}$  exceed  $30 \text{ cm day}^{-1}$  downwelling in CAR cyclones and  $40 \text{ cm day}^{-1}$  upwelling in CAR anticyclones.

The analysis in section 3 concluded that anomalies of the relative wind speed in the global composites are attributable to air–sea interaction over eddy-induced SST anomalies (Fig. 3). In regions such as the CAR where eddy SST anomalies are very small, however, perturbations of the relative wind measured by QuikSCAT are predominately generated by eddy surface currents and not by SST anomalies. For the CAR region, this hypothesis was tested by computing the relative wind speed anomalies for Gaussian eddies with representative amplitude, radius scale, and background wind speed and direction, but neglecting the SST effect on surface stress  $\tau$ . The magnitude and structure of the resulting relative wind speed anomalies (not shown here) are very similar to the observed relative wind speed anomalies of CAR eddies, especially for anticyclones. Secondary SST effects on relative wind speed are apparent in CAR cyclones, for which SST anomalies are larger in magnitude than for CAR anticyclones. Negative relative wind speed anomalies occur at the observed composite cyclonic eddy SSH extremum, in accord with what is expected from air–sea interaction over the cold cores of CAR cyclones. In addition, a secondary region of positive relative wind speed anomaly occurs to the east of the composite cyclonic eddy SSH extremum, collocated with a positive SST anomaly.

*c. The south Indian Ocean ( $20^\circ$ – $35^\circ$ S,  $80^\circ$ – $115^\circ$ E)*

Many of the eddies in the south Indian Ocean originate in the Leeuwin Current along the west coast of

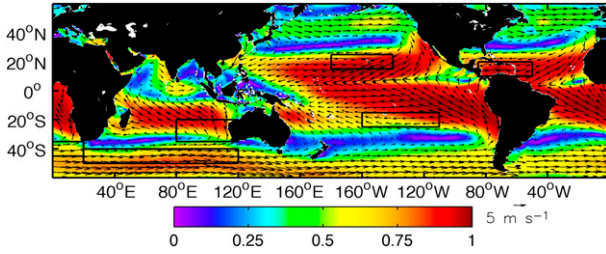


FIG. 12. Directional steadiness of the wind, defined to be the magnitude of the vector-averaged wind divided by the scalar-averaged wind speed, overlaid with vectors of the mean wind, computed from the QuikSCAT data. The averages were computed for the individual observations in all measurement swaths at each  $1/4^\circ$  grid point.

Australia (Gaube et al. 2013) and can be tracked as far west as  $50^\circ\text{E}$  (Fig. 11b). Here,  $W_{\text{SST}}$  is more than a factor of 6 smaller than  $W_{\text{cur}}$  (cf. Fig. 14e with Fig. 14d and note the different color bars). The estimated total

eddy-induced Ekman pumping  $\tilde{W}_{\text{tot}}$  is very similar to  $W_{\text{tot}}$  (Figs. 14c,f). Average total Ekman pumping magnitude in the SIO exceeds  $15 \text{ cm day}^{-1}$  in eddies of either polarity (Fig. 14c).

The dipolar structure of  $W_{\text{tot}}$  and  $\tilde{W}_{\text{tot}}$  (Figs. 14c,f) closely resembles that expected from the analysis of the idealized Northern Hemisphere Gaussian eddies in Fig. 6 with the following three exceptions: 1) The maximum upwelling velocities are located to the east of the eddy SSH extremum as a result of change in sign of  $W_\zeta$  in the Southern Hemisphere (see section 4b). 2) The axes of the asymmetric dipoles of Ekman pumping are oriented perpendicular to the predominately southeasterly winds in the SIO (Fig. 12). 3) The dipoles of Ekman pumping are more asymmetric in the SIO because of the spatial and temporal variability of the wind direction (Fig. 12), resulting in a “blurring” of the dipoles of  $W_\zeta$  in composite averages, thus allowing the monopole of  $W_c$  to increase the asymmetry of  $W_{\text{tot}}$  and  $\tilde{W}_{\text{tot}}$ .

## Caribbean Sea

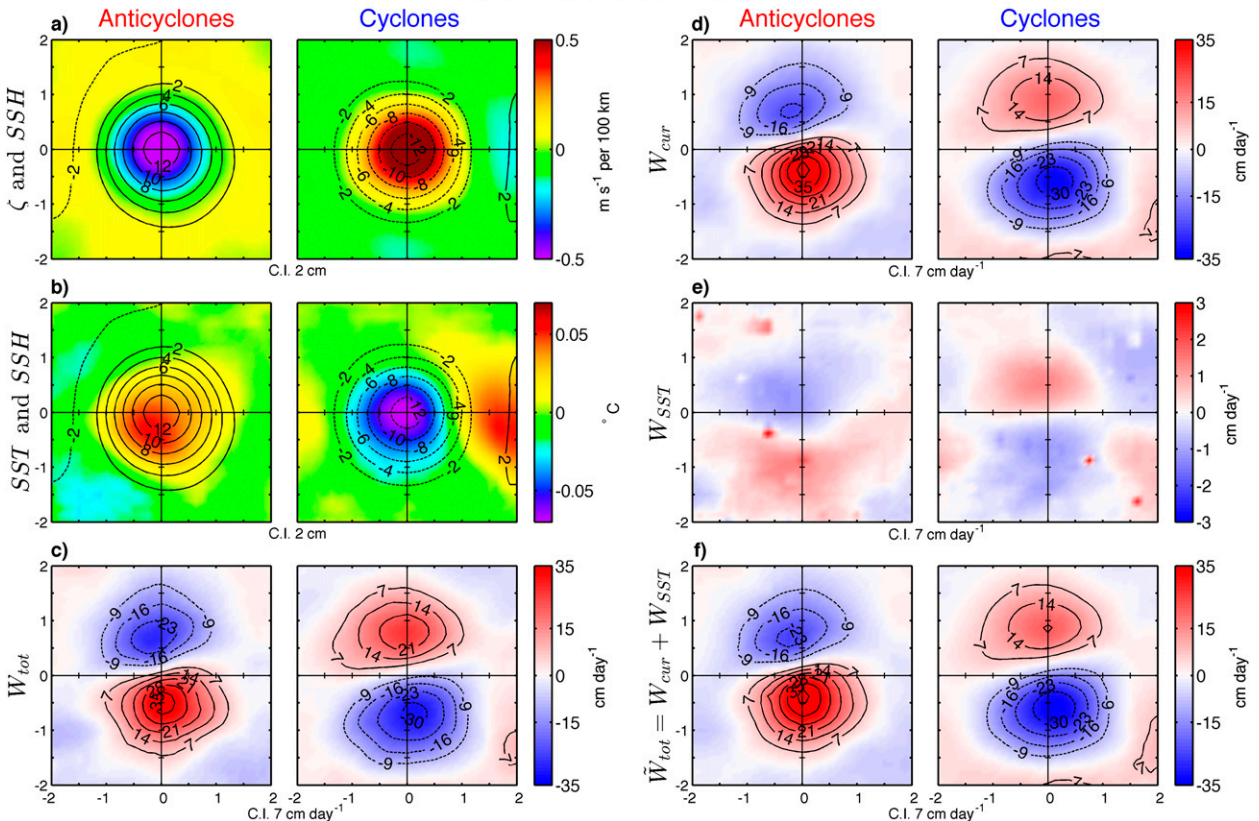


FIG. 13. Composite averages of eddies in the CAR region, defined as  $10^\circ\text{--}20^\circ\text{N}$  and  $275^\circ\text{--}310^\circ\text{E}$ . The  $x$  and  $y$  coordinates of the composite averages are normalized by the eddy scale  $L_s$ . Each pair of panels consists of composite averages for (left) anticyclones and (right) cyclones. Composite average of (a) geostrophic vorticity  $\zeta$  and contours of SSH. (b) SST anomalies and contours of SSH. (c) Eddy-induced Ekman pumping from QuikSCAT,  $W_{\text{tot}}$ . (d) Geostrophic surface current-induced Ekman pumping,  $W_{\text{cur}}$ . (e) SST-induced Ekman pumping,  $W_{\text{SST}}$ . (f) The estimated total Ekman pumping  $\tilde{W}_{\text{tot}}$  defined to be the sum of (d) and (e). Note the different colorbar scale for (e) compared with (c), (d), and (f).

## South Indian Ocean

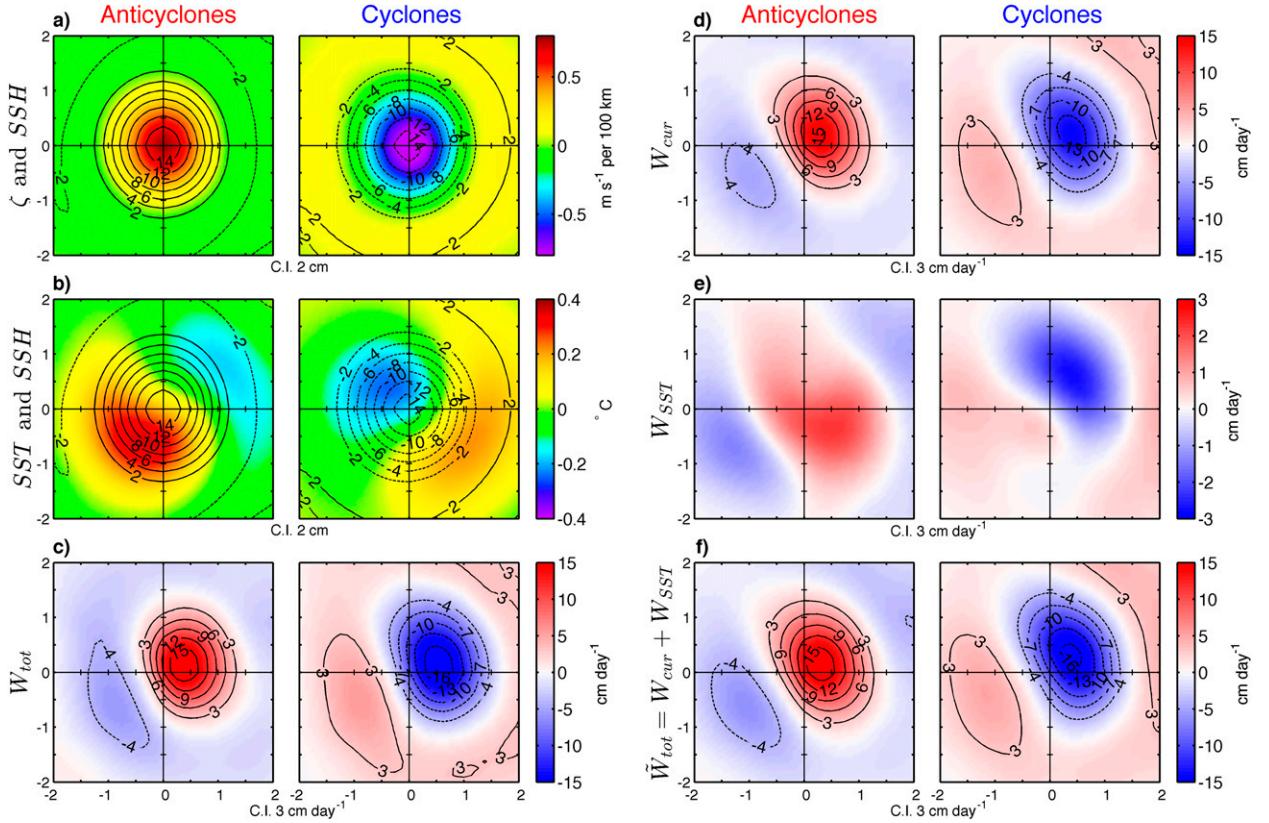


FIG. 14. As in Fig. 13, but for SIO (20°–35°S, 80°–115°E).

### *d. The Hawaiian Ridge (15°–25°N, 180°–220°E)*

The Hawaiian Ridge (HAW) is a region of energetic eddy variability (Chelton et al. 2011b). The altimetrically determined geostrophic currents associated with HAW eddies (Fig. 15a) generate  $W_{cur}$  (Fig. 15d) with structures similar to  $\bar{W}_{tot}$  and  $W_{tot}$  (Figs. 15c,f), implying that the total Ekman pumping is dominated by surface current effects. The trade winds in the HAW region are steady and east-northeasterly (Fig. 12), which results in dipoles of  $W_{tot}$ ,  $\bar{W}_{tot}$ , and  $W_{cur}$  that are elongated in the direction of the wind (Figs. 15c,d,f).

The SST anomalies of HAW anticyclones are characteristic of azimuthal advection of the ambient SST field around the eddy periphery (cf. Figs. 2 and 15b). The dipole SST anomalies for cyclones, however, are more asymmetric than for anticyclones (asymmetry ratio  $r = 1.3$  in anticyclones and  $r = 1.7$  in cyclones), and the axis of the dipoles is aligned more zonally. The structure of SST anomalies in cyclones is characteristic of the superposition of a dipole SST anomaly from horizontal advection of SST around the eddy and

a monopole of low SST associated with the uplifting of isopycnals within the eddy cores (Fig. 4).

SST-induced Ekman pumping  $W_{SST}$  in HAW eddies (Fig. 15e) is an order of magnitude weaker than  $W_{cur}$  (Fig. 15d). The different SST anomalies in HAW cyclones and anticyclones generate very different  $W_{SST}$ . In HAW anticyclones,  $W_{SST}$  is a monopole of upwelling centered just slightly to the north of the eddy center with weak sidelobes of Ekman downwelling to the north and southeast of the eddy center (Fig. 15e) that result from the interaction of the trade winds with the dipoles of SST (Fig. 15b). The SST anomalies in the interiors of HAW anticyclones generate perturbations in wind speed, resulting in a positive surface stress curl and Ekman upwelling. In cyclones, the primary negative pole of SST to the west of the eddy SSH extremum generates dipoles of  $W_{SST}$ , with the dipole axis oriented perpendicular to the easterly trade winds (Fig. 15e).

### *e. The South Pacific (15°–25°S, 200°–250°E)*

The eddies in the central South Pacific Ocean are relatively small in amplitude and large in horizontal



## Hawaiian Ridge

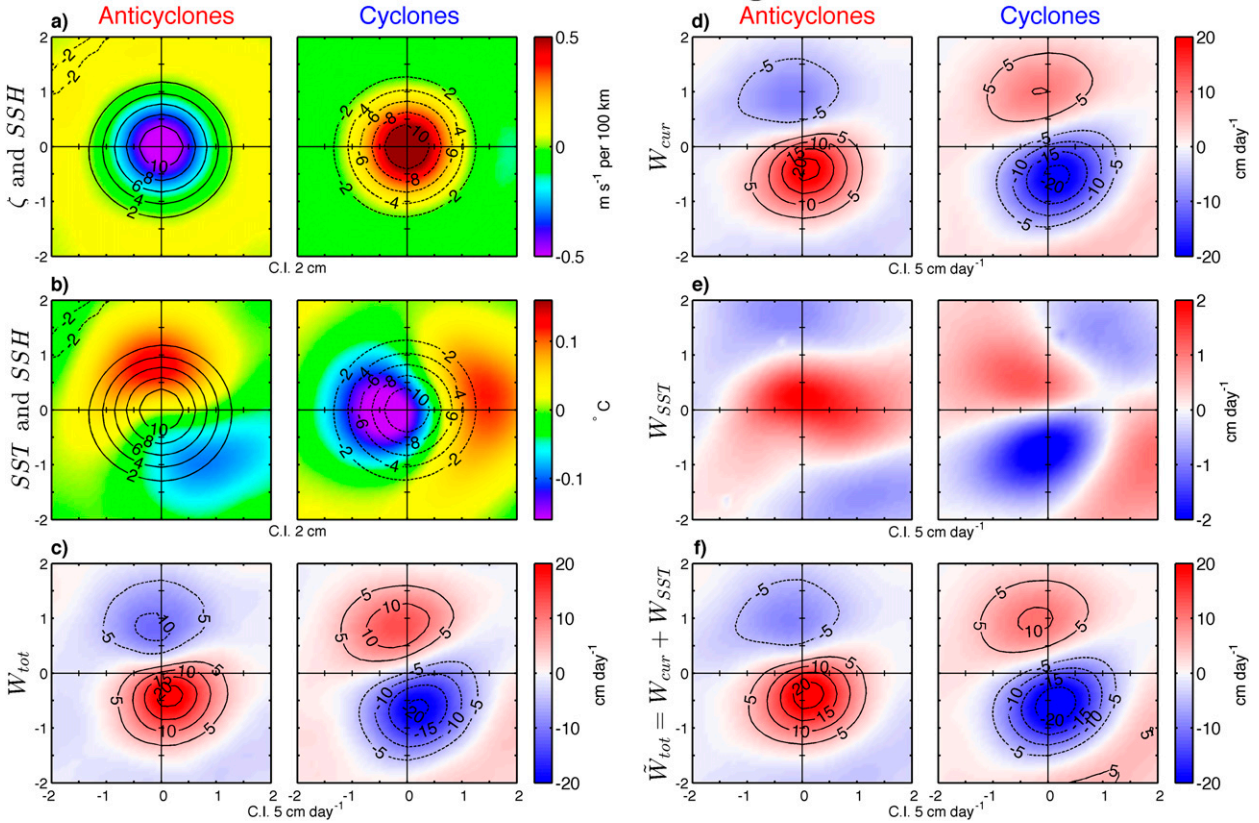


FIG. 15. As in Fig. 13, but for HAW ( $15^{\circ}$ – $25^{\circ}$ N,  $180^{\circ}$ – $220^{\circ}$ E).

scale (Figs. 1a,b; Table 1). Thus,  $W_{\text{cur}}$  is small compared with the eddies in the other regions considered above (see also Fig. 10a), although it is still about an order of magnitude stronger than  $W_{\text{SST}}$  (Figs. 16d,e) because of the small eddy-induced SST anomalies (Fig. 16b). The estimated total eddy-induced Ekman pumping  $\tilde{W}_{\text{tot}}$  from both SST and surface current effects (Fig. 16f) is therefore dominated by  $W_{\text{cur}}$  in Fig. 16d and is very similar to the observed  $W_{\text{tot}}$  in Fig. 16c.

The SST-induced Ekman pumping  $W_{\text{SST}}$  and current-induced Ekman pumping  $W_{\text{cur}}$  combine constructively in the SPO. Close inspection of Figs. 16c and 16f reveals that, while the primary poles of  $W_{\text{tot}}$  and  $\tilde{W}_{\text{tot}}$  are very similar in magnitude, the secondary poles of  $W_{\text{tot}}$  are somewhat larger in magnitude, resulting in less asymmetry than in  $\tilde{W}_{\text{tot}}$ . These small discrepancies could be a result of underestimation of the true SST-induced Ekman pumping because of the smoothing of SST in the objectively mapped SST fields noted in section 5.

In SPO eddies,  $W_{\text{tot}}$  exceeds  $8 \text{ cm day}^{-1}$  (Fig. 16c) that could result in an influx of nutrients into the cores of anticyclonic eddies. This influx of new nutrients as a result of the small but persistent upwelling in anticyclones

may account for the enhanced phytoplankton concentrations that are observed in the cores of SPO anticyclones (Gaube 2012; Gaube et al. 2014).

### f. The southeast Atlantic ( $35^{\circ}$ – $45^{\circ}$ S, $0^{\circ}$ – $20^{\circ}$ E)

Eddies in the southeast Atlantic region are highly energetic, with large amplitudes and rotational velocities (Table 1; Figs. 1a,b). These include the well-known Agulhas rings that form at the Agulhas Retroflection and sometimes propagate across the entire South Atlantic (Byrne et al. 1995; Schouten et al. 2000). Composite averages of current-induced Ekman pumping exceed  $20 \text{ cm day}^{-1}$  in anticyclones and  $10 \text{ cm day}^{-1}$  in cyclones (Fig. 17d). The larger magnitude of  $W_{\text{cur}}$  observed in SEA anticyclones is a result of eddies with amplitudes larger than approximately  $15 \text{ cm}$  being predominately anticyclonic in this region (Fig. 1a).

In contrast to the regions considered above, the SEA is a region of strong SST gradients that generate strong  $W_{\text{SST}}$ , comparable in magnitude to  $W_{\text{cur}}$  (Figs. 10a,b). SEA anticyclones have large composite average SST anomalies of nearly  $1^{\circ}\text{C}$  (Fig. 17b) that generate

## South Pacific Ocean

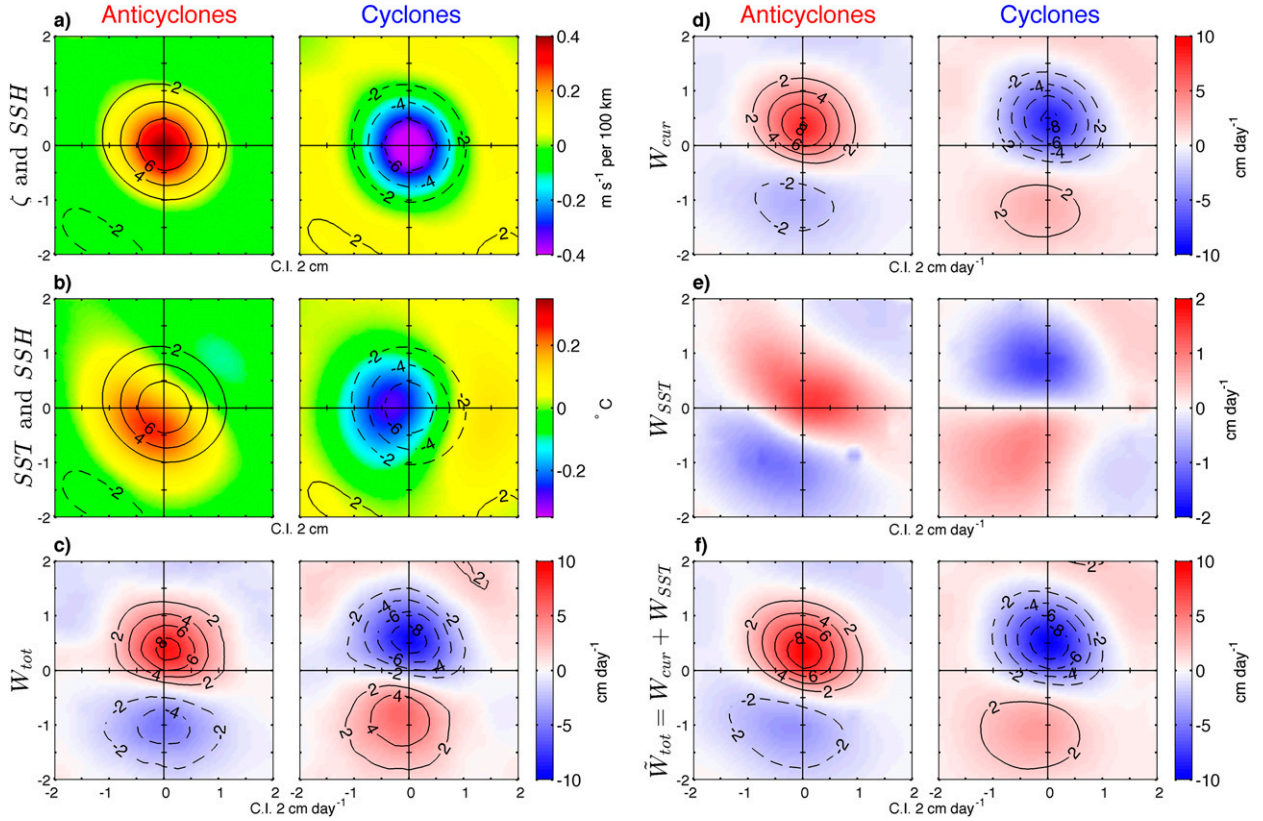


FIG. 16. As in Fig. 13, but for SPO (15°–25°S, 200°–250°E).

maximum  $W_{SST}$  of more than  $10 \text{ cm day}^{-1}$  centered approximately  $L_s$  to the south of the SSH extremum in anticyclones (Fig. 17e). Downwelling with slightly smaller magnitude occurs to the north of the SSH extremum of anticyclones. SST anomalies are smaller for SEA cyclones (Fig. 17b), resulting in  $W_{SST}$  of only  $-5 \text{ cm day}^{-1}$  to the south of the SSH extremum and  $4 \text{ cm day}^{-1}$  to the north (Fig. 17e).

The combination of large amplitudes (and hence strong rotational surface currents) and strong SST anomalies in SEA eddies generates total Ekman pumping anomalies with a geographic structure that is influenced by  $W_{SST}$  and  $W_{cur}$  (Fig. 17f). This is especially true for anticyclones because of their stronger SST anomalies (Fig. 17b). The  $W_{SST}$  and  $W_{cur}$  combine constructively (Figs. 17d–f), resulting in a southward displacement of maximum  $\tilde{W}_{tot}$  from the SSH extrema of both cyclones and anticyclones.

Estimates of  $\tilde{W}_{tot}$  and  $W_{tot}$  in SEA eddies have very similar spatial structures (Figs. 17c,f), but the magnitudes of  $\tilde{W}_{tot}$  are smaller than  $W_{tot}$ , possibly the result of underestimation of  $W_{SST}$ , as was discussed in

section 5. To test this possibility, we artificially increased  $\alpha_c^{strcr1}$  by 20%, resulting in new estimates of  $\tilde{W}_{tot}$  that were very similar to the  $W_{tot}$  observed by QuikSCAT. Underestimation of the SST gradient by this amount is plausible in regions where the scales of SST fronts are smaller than can be resolved in the objectively analyzed SST fields used here.

### *g. The Agulhas Return Current (40°–50°S, 20°–120°E)*

The mean winds over Agulhas Return Current are predominately westerly and exceed  $10 \text{ m s}^{-1}$  over much of the region (Fig. 12). The ARC is also a region of very strong SST gradients. The total Ekman pumping in ARC eddies is therefore expected to be influenced by both surface current and SST effects. This region is dominated by an intense eastward jetlike current, and some of the eddies identified in the ARC may in fact be slowly evolving meanders. Our consideration only of features with lifetimes of 12 weeks and longer is an attempt to focus primarily on isolated coherent vortices; meanders usually retain compact structures for time periods shorter than 12 weeks.



## Southeast Atlantic Ocean

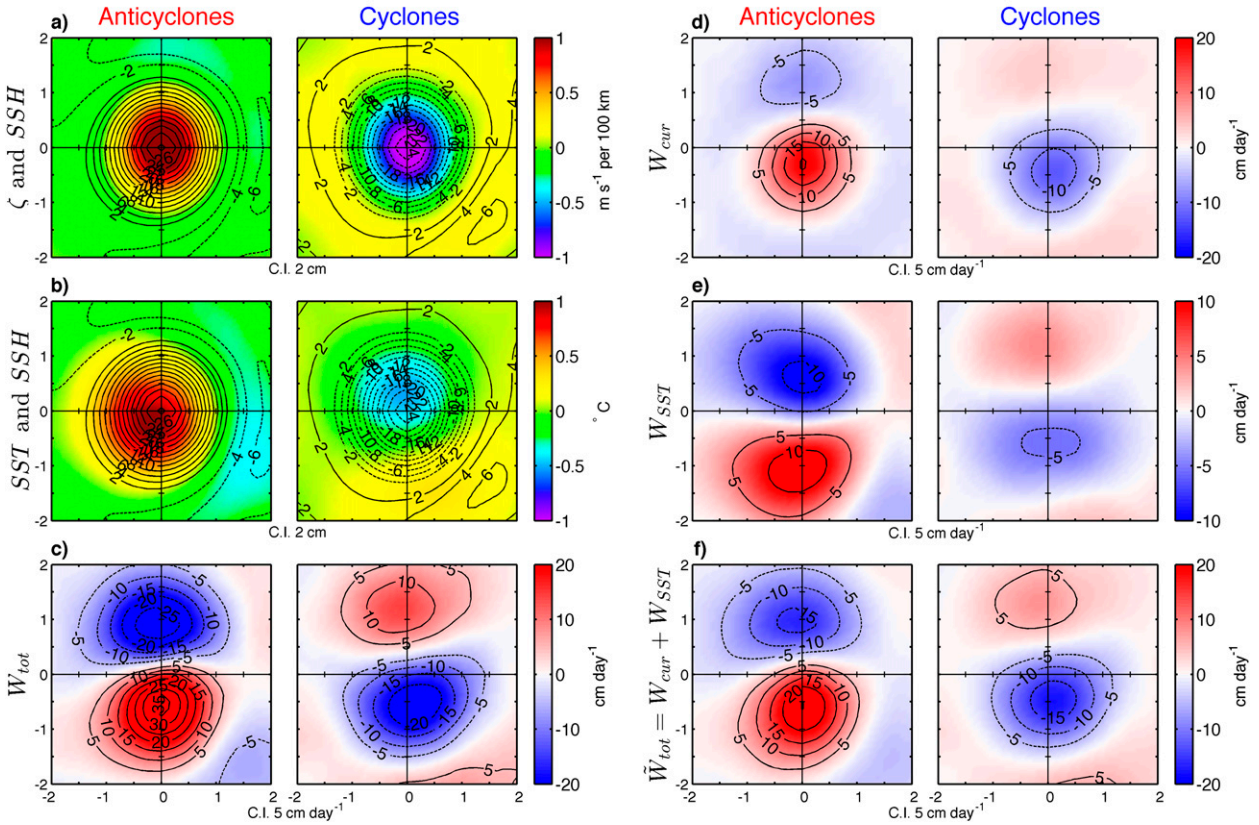


FIG. 17. As in Fig. 13, but for SEA ( $35^{\circ}$ – $45^{\circ}$ S,  $0^{\circ}$ – $20^{\circ}$ E).

Note, however, that surface currents and SST affect Ekman pumping within meanders in the same way as within mesoscale eddies.

Current-induced Ekman pumping  $W_{\text{cur}}$  in the ARC region has the expected asymmetric dipole structure with magnitudes that exceed  $15 \text{ cm day}^{-1}$ , with  $W_{\text{cur}}$  being slightly larger in magnitude in cyclones than anticyclones (Fig. 18d). This difference in the magnitude of  $W_{\text{cur}}$  is a result of slightly larger eddy amplitudes for cyclones in the ARC region (Table 1).

Eddies in the ARC generate SST anomalies that consist of monopoles centered approximately on their SSH extrema with slight southwestward displacement in anticyclones and northwestward displacement in cyclones (Fig. 18b). The associated  $W_{\text{SST}}$  (Fig. 18e) consists of dipoles with somewhat stronger upwelling (downwelling) on the south sides of anticyclones (cyclones). The combined influences of SST and currents are clearly evident in the composites of  $\tilde{W}_{\text{tot}}$  (Fig. 18f). The geographical structure of observed  $W_{\text{tot}}$  (Fig. 18c) is very similar to the estimated  $\tilde{W}_{\text{tot}}$  in Fig. 18f, except again with slightly smaller magnitude that likely results

from underestimation of the SST contribution to Ekman pumping, as discussed previously.

### 7. Attenuation of eddies as a result of Ekman pumping

The different contributions to the total current-induced Ekman pumping [(10)] influence the structure and kinematics of eddies in various ways. SST-induced Ekman pumping disrupts the approximate axisymmetric structure of eddies, thus tending to attenuate the eddies (Jin et al. 2009). The surface current vorticity gradient contribution  $W_{\zeta}$  generates asymmetric dipoles of Ekman upwelling and downwelling that tend to tilt the vertical axis of eddies (Stern 1965). The surface stress curl contribution  $W_c$  generates a monopole of Ekman pumping centered on the eddy core, which systematically attenuates eddy amplitudes (Dewar and Flierl 1987). In this section, we estimate the decay time scale of eddies as a result of  $W_c$ .

The decay time scale of geostrophic motions associated with Ekman pumping can be estimated from

## Agulhas Return Current

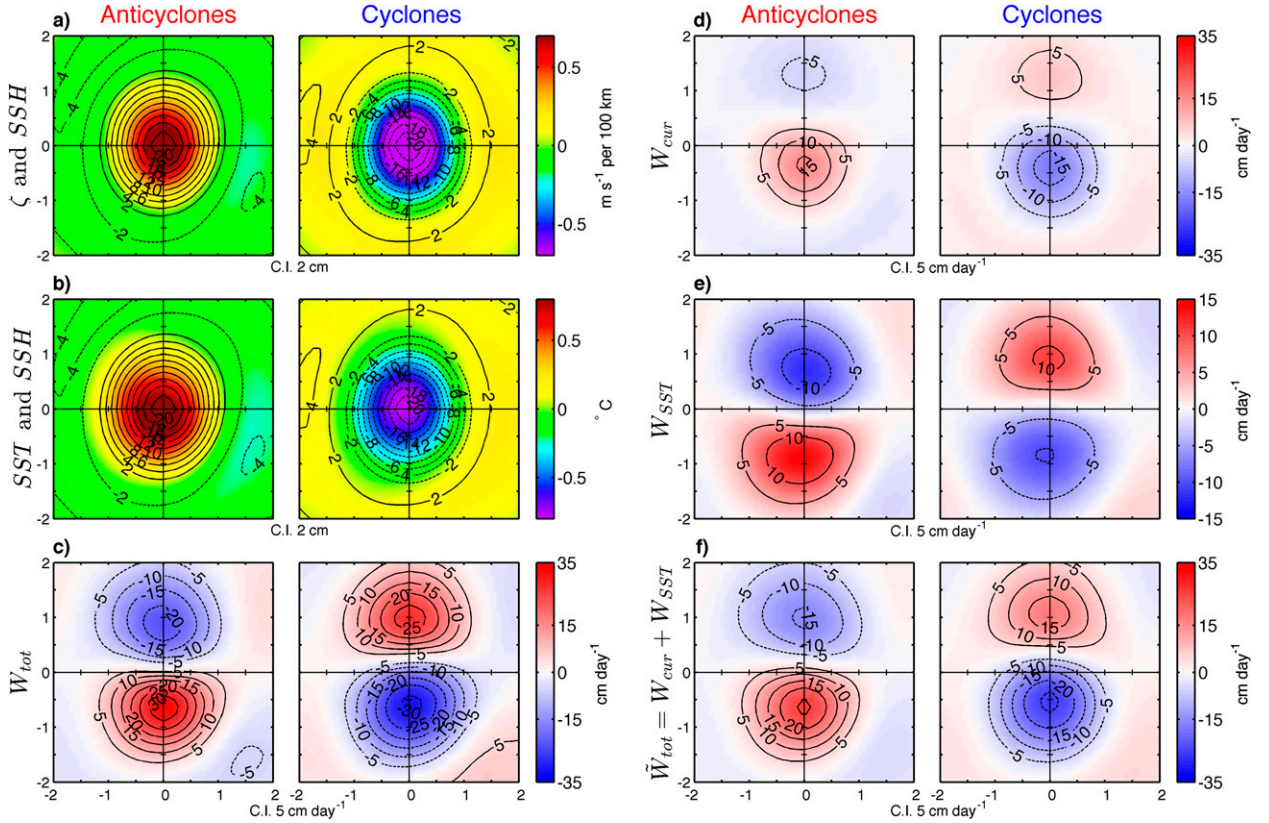


FIG. 18. As in Fig. 13, but for ARC (40°–50°S, 20°–120°E).

a simple vertically integrated barotropic vorticity balance:

$$D \frac{\partial \zeta}{\partial t} = -f W_c, \quad (14)$$

where  $D$  is the vertical scale of the eddy,  $\zeta$  is the relative vorticity of the current,  $f$  is the Coriolis parameter, and the surface stress curl contribution  $W_c$  to the total surface current-induced Ekman pumping is defined by (6). For mesoscale eddies with radii larger than  $\sim 20$  km, the correction of the total surface current-induced Ekman pumping by including  $\zeta$  in the denominators for mesoscale eddies is only  $O(10)\%$  for 80% of all midlatitude eddies (Fig. 7d). For the present purpose of deriving an order of magnitude estimate of the eddy attenuation time scale resulting from  $W_c$ , we therefore neglect  $\zeta$  in the denominator of (6) so that  $f + \zeta = f(1 + \zeta/f) \approx f$ , allowing  $W_c$  to be approximated by

$$\hat{W}_c = \frac{\mathbf{V} \times \tilde{\boldsymbol{\tau}}}{\rho_o f}, \quad (15)$$

where the hat signifies that  $\zeta$  has been omitted from the denominator.

A well-defined eddy decay time scale can be estimated from (14) if  $\hat{W}_c$  is proportional to  $\zeta$ . This is not the case in general. However, if the wind direction is assumed to be random, such a proportionality emerges. This is seen as follows: The background, large-scale absolute wind can be expressed as

$$\mathbf{u}_{bg} = U_a (\cos \theta, \sin \theta), \quad (16)$$

where  $\theta$  is the direction of the wind vector (0 for eastward), and  $U_a = \sqrt{u_{bg}^2 + v_{bg}^2}$  is the wind speed. Averaged over a uniform distribution of random wind directions  $0 < \theta < 2\pi$ , the mean surface stress  $\tilde{\boldsymbol{\tau}}$  from (9) for  $|\mathbf{u}_o| \ll U_a$  is approximately proportional to the surface currents:

$$\tilde{\boldsymbol{\tau}} = \frac{-3\rho_a C_D U_a (u_o, v_o)}{2}. \quad (17)$$

Substituting (17) into (15) reveals that, for these randomly directed large-scale winds, the corresponding mean  $\hat{W}_c$  is proportional to  $\zeta = \nabla \times \mathbf{u}_o$ ,

$$\hat{W}_c = \frac{-3\rho_a C_D U_a}{2\rho_o f} \zeta, \quad (18)$$

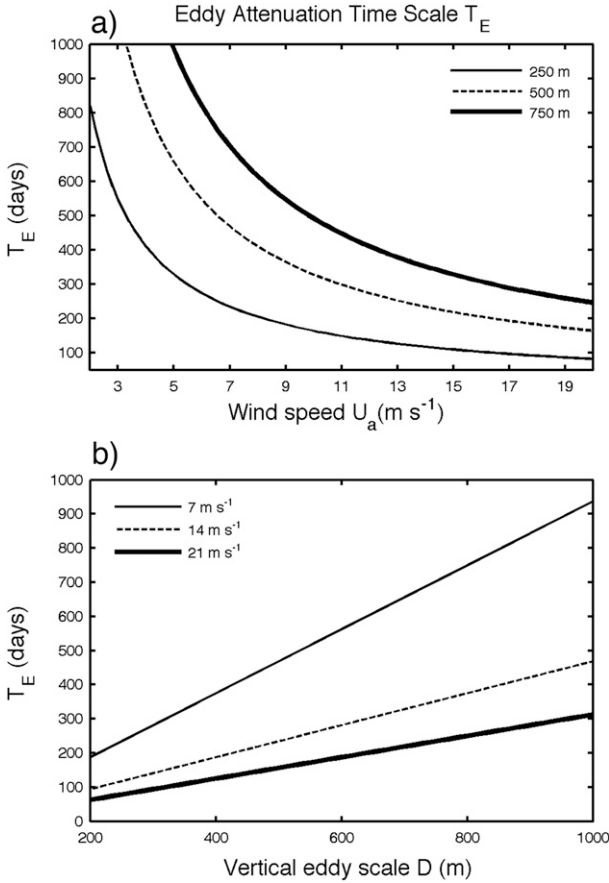


FIG. 19. Eddy attenuation time scale estimated by (19) as a function of (a) wind speed  $U_a$  for a series of eddy vertical scales  $D$  and (b) as a function of  $D$  for a series of different  $U_a$ . Nominal values of  $\rho_o = 1020 \text{ kg m}^{-3}$ ,  $\rho_a = 1.2 \text{ kg m}^{-3}$ , and  $C_D = 10^{-3}$  were used to compute the eddy attenuation time scale estimates.

and the eddy attenuation time scale becomes

$$T_E \sim \frac{2\rho_o D}{3\rho_a C_D U_a}. \quad (19)$$

Note that this estimate of eddy attenuation time scale depends only on the variable eddy vertical scale  $D$  and the large-scale wind speed  $U_a$  and not on the eddy amplitude  $A$  or radius  $L_s$ .

The eddy attenuation time scale  $T_E$  from (19) ranges from  $\sim 100$  to 1000 days, depending on  $D$  and  $U_a$  (Fig. 19). For an eddy with vertical scale  $D = 500 \text{ m}$  under a uniform  $U_a = 7 \text{ m s}^{-1}$  wind, assuming nominal values of the constants in (19), the decay time scale is 468 days (1.3 yr).

As the eddy decay time scale (19) depends linearly on the vertical scale  $D$ , further knowledge of the vertical structure of eddies is required for a rigorous estimate of the geographical variability of the eddy decay rate.

Moreover, the assumption of random wind direction frequently fails (e.g., Fig. 12) so that  $W_c$  is not proportional to  $\zeta$  and a direct quantitative estimate cannot be made. The above estimate of  $T_E$  as a function of the eddy vertical scale  $D$  and wind speed  $U_a$ , independent of eddy amplitude  $A$ , thus provides only a rough estimate of the eddy decay time scale.

## 8. Conclusions

The effects of surface currents and air–sea interaction associated with SST anomalies on eddy-induced Ekman pumping were investigated by isolating the Ekman pumping within oceanic mesoscale eddies. Current-induced Ekman pumping in eddies has been known to be important for several decades but SST effects have received relatively little attention. By collocating observations of SST to the interiors of midlatitude eddies, it was shown that eddies influence SST primarily by azimuthal advection in the presence of large-scale background SST gradients. The resulting eddy-induced SST gradients were shown to produce air–sea interaction with wind speed and surface stress curl perturbations that are consistent with those found in SST frontal regions.

An analysis of idealized eddies with realistic amplitudes, radii, and SST (section 6) showed that eddy-induced Ekman pumping is primarily caused by surface currents, with the SST contribution secondary. The magnitude of Ekman pumping resulting from surface current effects was shown to increase with eddy amplitude and to be inversely related to eddy radius scale.

The global composites in section 5 and regional composites in section 6 confirm observationally the conclusions of the analysis of idealized eddies in section 4: SST-induced Ekman pumping in mesoscale eddies is usually secondary to current-induced Ekman pumping. Exceptions to the general dominance of surface current effects occur in regions of strong SST gradients in regions of meandering zonal currents such as the Agulhas Return Current and the southeast Atlantic, where  $W_{\text{SST}}$  and  $W_{\text{cur}}$  are of similar magnitude.

The interactions between Ekman pumping, eddy kinematics, eddy dynamics, and nutrient cycling within eddies are complex. Since the  $\sim 10 \text{ cm day}^{-1}$  mesoscale eddy-induced Ekman pumping velocities are comparable to the basin-scale background Ekman pumping velocities from the large-scale surface stress curl fields (e.g., Risien and Chelton 2008), eddy-induced Ekman pumping is not negligible, especially since it is collocated with the interior of the eddy and is persistent over the lifetime of the eddy. The portion of the eddy-induced Ekman pumping from surface current effects is now being included in many ocean circulation models by



computing the surface stress from the relative vector wind defined by (3) that includes the influence of surface ocean currents (e.g., Duhaut and Straub 2006; Zhai and Greatbatch 2007; Eden and Dietze 2009; Hutchinson et al. 2010; McClean et al. 2011; Anderson et al. 2011).

Because the polarity of the eddy-induced curl of the surface stress is opposite that of the eddy, current-induced Ekman pumping systematically attenuates the eddies. It was shown in section 7 that the decay time scale of this attenuation is proportional to the vertical scale  $D$  of the eddy and to the large-scale, background wind speed  $U_a$ . A decay time scale of about 1.3 yr emerges for a typical wind speed of  $U_a = 7 \text{ m s}^{-1}$  and an eddy vertical scale of  $D = 500 \text{ m}$ .

Parameterizing the effects of air–sea interaction on the surface stress curl field to include the well-documented impact of SST perturbations on the wind is more complicated. This has been shown to be important in midlatitudes from empirically coupled modeling studies in idealized settings conducted by Jin et al. (2009) and Hogg et al. (2009). The inclusion of SST effects on the surface stress resulted in significant changes in the energetics of eddies (Jin et al. 2009) and on the large-scale ocean circulation (Hogg et al. 2009). By including the influence of both surface currents and eddy-induced SST perturbations on the surface stress curl, future modeling studies can assess what role the total eddy-induced Ekman pumping plays in eddy dynamics and in providing nutrients into the euphotic zone of the interiors of mesoscale eddies, as well as its effects on the large-scale circulation of the ocean.

**Acknowledgments.** We thank Remote Sensing Systems (<http://www.ssmi.com>) for providing the QuikSCAT vector wind observations, Collecte Localis Satellites, AVISO (<http://www.aviso.oceanobs.com>) for the SSH observations, and the NOAA National Climatic Data Center for the SST observations (data available at <ftp://eclipse.ncdc.noaa.gov/pub/OI-daily-v2/NetCDF>). We thank Martín S. Hoecker-Martínez for participating in valuable discussions during the writing of this manuscript. We also thank Dr. Peter Cornillon and an anonymous reviewer for comments that improved the manuscript. This work was funded by NASA Grants NNX08AI80G, NNX08AR37G, NNX13AD78G, NNX10AE91G, NNX13AE47G, and NNX10AO98G.

## REFERENCES

- Anderson, L., D. McGillicuddy, M. Maltrud, I. Lima, and S. Doney, 2011: Impact of eddy–wind interaction on eddy demographics and phytoplankton community structure in a model of the North Atlantic Ocean. *Dyn. Atmos. Oceans*, **52**, 80–94, doi:10.1016/j.dynatmoce.2011.01.003.
- Byrne, D. A., A. L. Gordon, and W. F. Haxby, 1995: Agulhas eddies: A synoptic view using Geosat ERM data. *J. Phys. Oceanogr.*, **25**, 902–917, doi:10.1175/1520-0485(1995)025<0902:AEASVU>2.0.CO;2.
- Chelton, D., and M. Freilich, 2005: Scatterometer-based assessment of 10-m wind analyses from the operational ECMWF and NCEP numerical weather prediction models. *Mon. Wea. Rev.*, **133**, 409–429, doi:10.1175/MWR-2861.1.
- , and S. Xie, 2010: Coupled ocean–atmosphere interaction at oceanic mesoscales. *Oceanography*, **23**, 52–69, doi:10.5670/oceanog.2010.05.
- , M. Schlax, M. Freilich, and R. Milliff, 2004: Satellite measurements reveal persistent small-scale features in ocean winds. *Science*, **303**, 978–983, doi:10.1126/science.1091901.
- , P. Gaube, M. Schlax, J. Early, and R. Samelson, 2011a: The influence of nonlinear mesoscale eddies on near-surface oceanic chlorophyll. *Science*, **334**, 328–332, doi:10.1126/science.1208897.
- , M. Schlax, and R. Samelson, 2011b: Global observations of nonlinear mesoscale eddies. *Prog. Oceanogr.*, **91**, 167–216, doi:10.1016/j.pocean.2011.01.002.
- Chow, C., and Q. Liu, 2012: Eddy effects on sea surface temperature and sea surface wind in the continental slope region of the northern South China Sea. *Geophys. Res. Lett.*, **39**, L02601, doi:10.1029/2011GL050230.
- Cornillon, P., and K. Park, 2001: Warm core ring velocities inferred from NSCAT. *Geophys. Res. Lett.*, **28**, 575–578, doi:10.1029/2000GL011487.
- Dewar, W., and G. Flierl, 1987: Some effects of the wind on rings. *J. Phys. Oceanogr.*, **17**, 1653–1667, doi:10.1175/1520-0485(1987)017<1653:SEOTWO>2.0.CO;2.
- Ducet, N., P.-Y. Le Traon, and G. Reverdin, 2000: Global high-resolution mapping of ocean circulation from TOPEX/Poseidon and ERS-1 and-2. *J. Geophys. Res.*, **105**, 19 477–19 498, doi:10.1029/2000JC900063.
- Duhaut, T. H., and D. N. Straub, 2006: Wind stress dependence on ocean surface velocity: Implications for mechanical energy input to ocean circulation. *J. Phys. Oceanogr.*, **36**, 202–211, doi:10.1175/JPO2842.1.
- Eden, C., and H. Dietze, 2009: Effects of mesoscale eddy/wind interactions on biological new production and eddy kinetic energy. *J. Geophys. Res.*, **114**, C05023, doi:10.1029/2008JC005129.
- Fairall, C., E. Bradley, J. Hare, A. Grachev, and J. Edson, 2003: Bulk parameterization of air–sea fluxes: Updates and verification for the COARE algorithm. *J. Climate*, **16**, 571–591, doi:10.1175/1520-0442(2003)016<0571:BPOASF>2.0.CO;2.
- Frenger, I., N. Gruber, R. Knutti, and M. Münnich, 2013: Imprint of Southern Ocean eddies on winds, clouds and rainfall. *Nat. Geosci.*, **6**, 608–612, doi:10.1038/ngeo1863.
- Gaube, P., 2012: Satellite observations of the influence of mesoscale ocean eddies on near-surface temperature, phytoplankton and surface stress. Ph.D. thesis, Oregon State University, 197 pp. [Available from 104 CEOAS Admin. Bldg., Corvallis, OR 97331.]
- , D. Chelton, P. Strutton, and M. Behrenfeld, 2013: Satellite observations of chlorophyll, phytoplankton biomass, and Ekman pumping in nonlinear mesoscale eddies. *J. Geophys. Res. Oceans*, **118**, 6349–6370, doi:10.1002/2013JC009027.
- , D. McGillicuddy Jr., D. Chelton, M. Behrenfeld, and P. Strutton, 2014: Regional variations in the influence of mesoscale eddies on near-surface chlorophyll. *J. Geophys. Res. Oceans*, doi:10.1002/2014JC010111, in press.



- Hausmann, U., and A. Czaja, 2012: The observed signature of mesoscale eddies in sea surface temperature and the associated heat transport. *Deep-Sea Res. I*, **70**, 60–72, doi:[10.1016/j.dsr.2012.08.005](https://doi.org/10.1016/j.dsr.2012.08.005).
- Hogg, A., W. Dewar, P. Berloff, S. Kravtsov, and D. Hutchinson, 2009: The effects of mesoscale ocean–atmosphere coupling on the large-scale ocean circulation. *J. Climate*, **22**, 4066–4082, doi:[10.1175/2009JCLI2629.1](https://doi.org/10.1175/2009JCLI2629.1).
- Hutchinson, D. K., A. M. C. Hogg, and J. R. Blundell, 2010: Southern Ocean response to relative velocity wind stress forcing. *J. Phys. Oceanogr.*, **40**, 326–339, doi:[10.1175/2009JPO4240.1](https://doi.org/10.1175/2009JPO4240.1).
- Jin, X., C. Dong, J. Kurian, J. McWilliams, D. Chelton, and Z. Li, 2009: SST–wind interaction in coastal upwelling: Oceanic simulation with empirical coupling. *J. Phys. Oceanogr.*, **39**, 2957–2970, doi:[10.1175/2009JPO4205.1](https://doi.org/10.1175/2009JPO4205.1).
- Large, W. G., J. C. McWilliams, and S. C. Doney, 1994: Oceanic vertical mixing: A review and a model with a nonlocal boundary layer parameterization. *Rev. Geophys.*, **32**, 363–403, doi:[10.1029/94RG01872](https://doi.org/10.1029/94RG01872).
- Ledwell, J., D. McGillicuddy Jr., and L. Anderson, 2008: Nutrient flux into an intense deep chlorophyll layer in a mode-water eddy. *Deep-Sea Res. II*, **55**, 1139–1160, doi:[10.1016/j.dsr2.2008.02.005](https://doi.org/10.1016/j.dsr2.2008.02.005).
- Leetmaa, A., and A. F. Bunker, 1978: Updated charts of the mean annual wind stress, convergences in the Ekman layers, and Sverdrup transports in the North Atlantic. *J. Mar. Res.*, **36**, 311–322.
- Liu, W. T., and W. Tang, 1996: Equivalent neutral wind. National Aeronautics and Space Administration/Jet Propulsion Laboratory/California Institute of Technology JPL Publ. 96-17, 22 pp. [Available online at <http://ntrs.nasa.gov/archive/nasa/casi.ntrs.nasa.gov/19970010322.pdf>.]
- Lucrezia, R., and F. Wentz, 2011: Reprocessed QuikSCAT (V04) wind vectors with Ku-2011 geophysical model function. Remote Sensing Systems Tech. Rep. 042011, 8 pp.
- Martin, A., and K. Richards, 2001: Mechanisms for vertical nutrient transport within a North Atlantic mesoscale eddy. *Deep-Sea Res. II*, **48**, 757–773, doi:[10.1016/S0967-0645\(00\)00096-5](https://doi.org/10.1016/S0967-0645(00)00096-5).
- McClean, J., and Coauthors, 2011: A prototype two-decade fully-coupled fine-resolution CCSM simulation. *Ocean Modell.*, **39**, 10–30, doi:[10.1016/j.ocemod.2011.02.011](https://doi.org/10.1016/j.ocemod.2011.02.011).
- McGillicuddy, D., and Coauthors, 2007: Eddy/wind interactions stimulate extraordinary mid-ocean plankton blooms. *Science*, **316**, 1021–1026, doi:[10.1126/science.1136256](https://doi.org/10.1126/science.1136256).
- , J. Ledwell, and L. Anderson, 2008: Response to comments on “Eddy/wind interactions stimulate extraordinary mid-ocean plankton blooms.” *Science*, **320**, 488, doi:[10.1126/science.1148974](https://doi.org/10.1126/science.1148974).
- O’Neill, L. W., 2012: Wind speed and stability effects on coupling between surface wind stress and SST observed from buoys and satellite. *J. Climate*, **25**, 1544–1569, doi:[10.1175/JCLI-D-11-00121.1](https://doi.org/10.1175/JCLI-D-11-00121.1).
- , D. B. Chelton, S. K. Esbensen, and F. J. Wentz, 2005: High-resolution satellite measurements of the atmospheric boundary layer response to SST variations along the Agulhas Return Current. *J. Climate*, **18**, 2706–2723, doi:[10.1175/JCLI3415.1](https://doi.org/10.1175/JCLI3415.1).
- , —, and —, 2010: The effects of SST-induced surface wind speed and direction gradients on midlatitude surface vorticity and divergence. *J. Climate*, **23**, 255–281, doi:[10.1175/2009JCLI2613.1](https://doi.org/10.1175/2009JCLI2613.1).
- , —, and —, 2012: Covariability of surface wind and stress responses to sea surface temperature fronts. *J. Climate*, **25**, 5916–5942, doi:[10.1175/JCLI-D-11-00230.1](https://doi.org/10.1175/JCLI-D-11-00230.1).
- Park, K., and P. Cornillon, 2002: Stability-induced modification of sea surface winds over Gulf Stream rings. *Geophys. Res. Lett.*, **29**, 2211, doi:[10.1029/2001GL014236](https://doi.org/10.1029/2001GL014236).
- , —, and D. Codiga, 2006: Modification of surface winds near ocean fronts: Effects of Gulf Stream rings on scatterometer (QuikSCAT, NSCAT) wind observations. *J. Geophys. Res.*, **111**, C03021, doi:[10.1029/2005JC003016](https://doi.org/10.1029/2005JC003016).
- Reynolds, R. W., and D. B. Chelton, 2010: Comparisons of daily sea surface temperature analyses for 2007–08. *J. Climate*, **23**, 3545–3562, doi:[10.1175/2010JCLI3294.1](https://doi.org/10.1175/2010JCLI3294.1).
- , T. Smith, C. Liu, D. Chelton, K. Casey, and M. Schlax, 2007: Daily high-resolution-blended analyses for sea surface temperature. *J. Climate*, **20**, 5473–5496, doi:[10.1175/2007JCLI1824.1](https://doi.org/10.1175/2007JCLI1824.1).
- Risien, C., and D. Chelton, 2008: A global climatology of surface wind and wind stress fields from eight years of QuikSCAT scatterometer data. *J. Phys. Oceanogr.*, **38**, 2379–2413, doi:[10.1175/2008JPO3881.1](https://doi.org/10.1175/2008JPO3881.1).
- Ross, D., J. Overland, W. Plerson, V. Cardone, R. McPherson, and T. Yu, 1985: Chapter 4 oceanic surface winds. *Advances in Geophysics*, Vol. 27, Academic Press, 101–140, doi:[10.1016/S0065-2687\(08\)60404-5](https://doi.org/10.1016/S0065-2687(08)60404-5).
- Schouten, M. W., W. P. Ruijter, P. J. Leeuwen, and J. R. Lutjeharms, 2000: Translation, decay and splitting of Agulhas rings in the southeastern Atlantic Ocean. *J. Geophys. Res.*, **105**, 21 913–21 925, doi:[10.1029/1999JC000046](https://doi.org/10.1029/1999JC000046).
- Small, R., S. Xie, and J. Hafner, 2005: Satellite observations of mesoscale ocean features and copropagating atmospheric surface fields in the tropical belt. *J. Geophys. Res.*, **110**, C02021, doi:[10.1029/2004JC002598](https://doi.org/10.1029/2004JC002598).
- , and Coauthors, 2008: Air–sea interaction over ocean fronts and eddies. *Dyn. Atmos. Oceans*, **45**, 274–319, doi:[10.1016/j.dynatmoce.2008.01.001](https://doi.org/10.1016/j.dynatmoce.2008.01.001).
- Stern, M., 1965: Interaction of a uniform wind stress with a geostrophic vortex. *Deep-Sea Res. Oceanogr. Abstr.*, **12**, 355–367, doi:[10.1016/0011-7471\(65\)90007-0](https://doi.org/10.1016/0011-7471(65)90007-0).
- Zhai, X., and R. J. Greatbatch, 2007: Wind work in a model of the northwest Atlantic Ocean. *Geophys. Res. Lett.*, **34**, L04606, doi:[10.1029/2006GL028907](https://doi.org/10.1029/2006GL028907).